Molten Salt Reactor Experiment

Dynamic Xenon Model

Design Report

Terry J Price

Terry doht Price aht UOIT doht net

2019/08/09

This version was compiled on 2019/08/09 at 04:53:00

I

II

Statement of Contributions

I hereby declare that all work in this thesis is my own except for:

- The Serpent 2 model of the MSRE which was developed by Gavin Ridley of University of Tennessee, Knoxville, as an undergraduate thesis project.

- The idea for doing the second order solution to the reaction diffusion equation graphite stringer model used in the dynamic model was given by Scott Greenwood, staff at the Oak Ridge National Laboratory, after a failed first attempt using a first order method.

- The background and theory, albeit written in my own words, were paraphrased from numerous sources I have read over the years. I am unsure as to how to appropriately cite something that is said in a large number of books.

Contents

List of Figures

List of Tables

CHAPTER 1

Background and Theory

1.1 Reactor Physics

1.1.1 Nuclear Fission

The atomic theory of matter states that all matter is made of sub nano meter particles called atoms. Within the atom is a dense region of *matter* (albeit the word *matter* begin to break down at the point) called the *nucleus*. The nucleus is comprised of positively charged *protons* and neutral *neutrons* and is about a femto (1×10^{-15} m) in scale.

A nucleus may split in two or more pieces in a process called *fission*. The most common way to induce fission in engineering applications is through a free neutron. Since neutrons are neutral, they do not interact with the target nucleus through electric forces and therefore retain their velocity until impact. The impact and subsequent absorption of a neutron can impart sufficient energy into the target nucleus that it splits apart in fission.

Nuclear fission produces a number of *fission products*, which include:

- bound clusters of protons and neutrons known as fission fragments;

- high energy photons which are gamma radiation;

- free neutrons

The fission products of a nucleus that has undergone fission have a net weight less than the original nucleus. This is because a portion of the matter from the original nucleus has been transformed into energy through Einstein's mass / energy equivalence principle,

$$E = mc^2. \tag{1.1}$$

This energy is distributed to the fission products and is extracted from nuclear fuel through the working fluid of a nuclear reactor.

Since free neutrons are also released in nuclear fission this can induce a *chain reaction* in nuclear fuel and it is the exploitation of this chain reaction mechanism that has given rise to the nuclear reactor.

1.1.2   Radioactive Decay

An atom's particular nuclear configuration gives it a certain level of tendency to remain in its current configuration — stability. An atom may reconfigure itself through the process of *radioactive decay*. The three predominate modes of decay are:

- Alpha decay – emission of a helium nucleus

- Beta (minus) decay – transmutation of a proton in a neutron and the subsequent emission of an electron

- Gamma decay – deexcitation of the nucleus through the emission of a high energy photon

Each of these decay modes reconfigure the transmuting nucleus into a more stable configuration.

Each decay mode has associated with it a *Decay Constant*, which is defined as the negative of the rate of change of a radioactive isotope per atom,

$$-\lambda \stackrel{def.}{=} \frac{1}{N} \frac{dN}{dt}.$$ (1.2)

A closely related concept is the radioactive half life which is defined as the amount of time it takes a population of atoms to reduce by a factor of two,

$$t_{1/2} \stackrel{def.}{=} t \quad : \quad 2N(t = t_{1/2}) = N(t = t_0).$$ (1.3)

Finally, we note that a particular atom may undergo consecutive radioactive decays and the series of isotopes the atom transmutes into is called its *decay chain.*

1.1.3   Neutron Interaction With Matter

Since neutrons are neutrally charged, they do not interact with an atom's electric cloud and only interact with the nucleus of an atom. Because of this, neutrons can pass through large amounts of matter without interacting and the interaction of neutrons with matter is described through probability theory.

Neutrons may interact with matter in numerous different ways. Examples include scattering, alpha production, absorption, and fission. The two modes of interaction we are concerned with in this thesis are fission and absorption. Fission has already been described. Neutron absorption is where a neutron is absorbed by a target nucleus.

The probability a neutron undergoes interaction of type i in matter per unit distance traveled in matter is called its *macroscopic cross section*, Σ_i and is

defined,

$$\Sigma_i \overset{def.}{=} \frac{dR_i}{dx} \tag{1.4}$$

The macroscopic neutron absorption cross section is written Σ_a, and the macroscopic neutron fission cross section is written Σ_f.

The interaction of a neutron with a nucleus can be conceptualized as firing a *dart* at a target with a cross sectional area σ. If the dart lands within the target with area σ_i, the target nucleus undergoes a reaction of type i. This quantity is known as the microscopic cross section and through proofs shown in numerous text books is related to the macroscopic cross section by the product of the microscopic cross section and the number density of atoms in a substance,

$$\Sigma_i = N\sigma_i. \tag{1.5}$$

In order for the parameterization of neutronic interaction with matter to be complete, we need to also define a quantity which describes the rate at which neutrons pass through matter. For this, consider a sphere of unit surface area. The rate at which neutrons pass through the surface of this sphere, in either direction, is called the neutron flux ,ϕ, and it is the product of neutron flux and the macroscopic cross section that gives the reaction rate per unit volume for neutrons in a substance,

$$R_i = \Sigma_i\phi. \tag{1.6}$$

Finally, we note that a fission only produces a finite number of fission fragments. As a result, each isotope, i, has a certain probability of being produced, γ_i, which is called the *fission yield* of isotope i. Therefore, if we want to determine the volumetric rate of production of a particular isotope, we multiply the fission

yield by the yield of that isotope,

$$\dot{N}_i = \gamma_i \Sigma_f \phi. \tag{1.7}$$

1.2 Molten Salt Reactors

1.2.1 The Working Principle of Fluid Fuel Reactors

Molten salt reactors (MSRs) are a type of nuclear reactor that contains, controls, and collects energy from a chain reaction and through continuous cooling of the nuclear fuel. Unlike a solid fuel reactor, where the nuclear fuel remains relatively stationary under nominal operating conditions, the nuclear fuel in a molten salt reactor circulates in a fuel salt that acts as both the primary working fluid and the fuel matrix.

An illustration of a molten salt reactor in shown in Figure 1.1. The corresponding flow path for the diagram is shown in Figure 1.2. The fuel salt circulates in the *primary loop* between the reactor core and the heat exchanger (9), with inertia imparted to it via a fuel pump (10). In this way, the reactor may be partitioned into in-core and out-of-core regions. Furthermore, the total system of both the in-core and out-of-core regions is referred to, in general, as the *reactor*. The fuel salt enters the in-core region through an inlet (13) and proceeds down a downcomer (12) into the lower plenum (11) whereupon it moves up a set of fuel channels (1) cut into blocks of graphite, referred to as graphite stringers (2). Note, the graphite stringers are formed of a porous matrix of graphite which have both a gaseous pore-space and a solid matrix component. Once past the graphite stringers, the fuel salt enters into the upper plenum (7), which has an interface to a cover gas region (5), before heading out the reactor outlet (14), and entering the out-of-core region. The totality of the graphite

stringers is referred to as the graphite moderator or moderating region. It is
when the fuel salt is within this moderating region that free neutrons become
sufficiently thermalized to induced nuclear fission and thereby generate heat.
Once the fuel salt has left the outlet, it enters the out-of-core region, where-
upon the heat generated in fission is transferred to a secondary working fluid
through a heat exchanger. Optionally, the fuel salt may pass through a *xenon
stripper* (not depicted) as it transitions between the in-core and out-of-core re-
gions.[1] No work has been found which standardizes any MSR terminology. One
additional aspect that is highly important to the analysis of xenon in MSRs is
the existence of circulating bubbles (not depicted), also called circulating voids,
within the fuel salt.

---

[1]Eades, Chaleff, Venneri, and Blue called these region in-core and ex-core in their 2016
paper. [1]
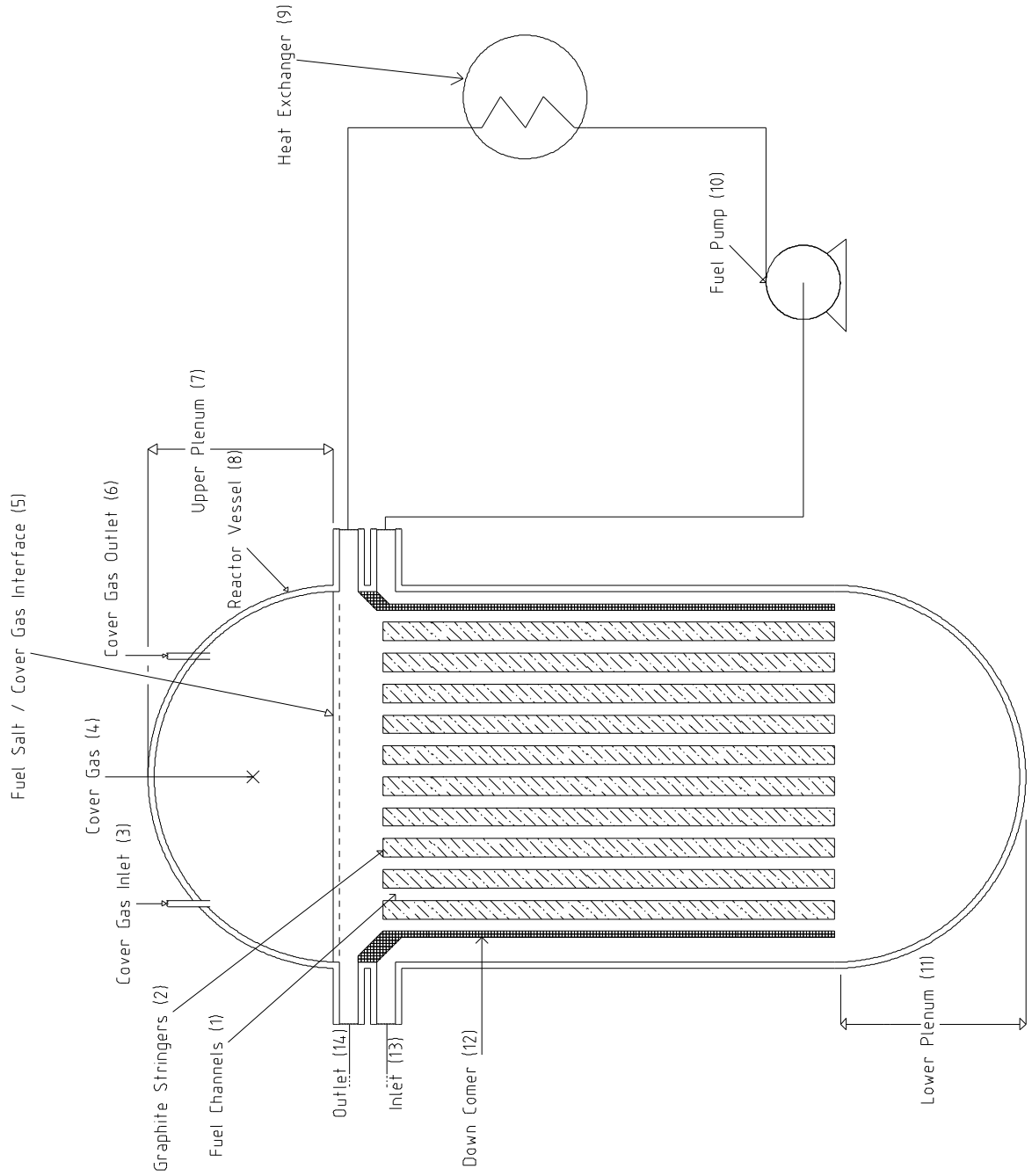
Figure 1.1: Diagram of a molten salt reactor
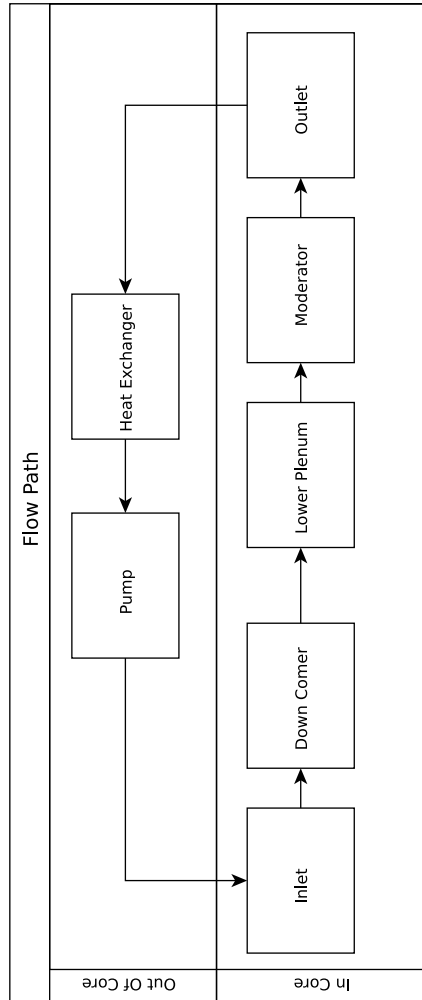
Figure 1.2: Diagram of a molten salt reactor

1.2.2 Previous Reactors

There have been three molten salt reactors built to date:

- the Aircraft Reactor Experiment (ARE)[2], a $2.5\,\mathrm{MW}_{th}$ experimental propulsion unit for use in a nuclear power bomber aircraft – operated in 1954,

- the Pratt and Whitney Aircraft Reactor 1 (PWAR-1), a zero-power experimental pile – operated in 1957,

- the Molten Salt Reactor Experiment (MSRE) A $7.4\,\mathrm{MW}_{\mathrm{th}}$ experimental reactor – operated 1964-1969.

All of these reactors were operated at Oak Ridge National Laboratory (ORNL) in Oak Ridge, Tennessee and are experimental (not production designs).

In addition to these three reactors there were additional research efforts, which never reached the construction phase. These *paper reactors* include:

- the Molten Salt Fast Reactors (MSFRs), fast-spectrum MSRs, reported in 1956,

- the Molten Salt Breeder Reactors (MSBRs), a series of breeding MSRs, including a single and dual fluid variety, reported in 1966,

- the Molten Salt Demonstration Reactor (MSDR), a $350\,\mathrm{MW}_e$ power producing reactor, reported in 1971,

- the Denatured Molten Salt Reactor (DMSR), a 1000 MW_e proliferation resistant molten reactor reported in 1980.

Roughly speaking, there have been three distinct phases of MSR development. The first phase, which lasted roughly from 1953-1959 was primarily focused on the development of MSRs for military aircraft propulsion. Key projects

---

[2]Note: some literature was found which appear to refer to the ARE as the *Fused Salt Reactor Experiment*

in this first phase included the ARE and PWAR-1 reactors. Many development activities were military in origin or under the auspices of the Atomic Energy Commission (AEC). The second era of MSR development activities was focused on civilian applications of MSRs and lasted roughly from 1960-1980. During this time, the MSRE was developed, and conceptual work was done on the MSBRs; this era concluded with work on the DMSR. In the period between 1980 to 2000, comparatively little work was done in the field of MSRs. On the subject of the discontinuation of the MSR at Oak Ridge National Laboratory, Alvin Weinberg, the director of the lab during much of its involvement with the MSRs, wrote in his 1994 autobiography,

"Why didn't the molten-salt system, so elegant and so well thought-out prevail? I've already given the political reason: that the fast breeder arrived first and was therefore able to consolidate its political position within the AEC. But there was another, more technical reason. The molten-salt technology is entirely different from the technology of any other reactor. To the inexperienced, molten-salt technology is daunting. This certainly seemed to be Milton Shaw's attitude towards molten salts – and he after all was the director of reactor development at the AEC during the molten-salt development. Perhaps the moral to be drawn is that a technology that differs too much from an existing technology has not one hurdle to overcome – to demonstrate its feasibility – but another, even greater one – to convince influential individuals and organizations who are intellectually and emotionally attached to a different technology that they should adopt the new path. This, the molten-salt system could not do. It was a successful technology that was dropped because it was too different from the main lines of reactor development. But if

weakness in other systems are eventually revealed, I hope that in a second nuclear era, the molten-salt technology will be resurrected."

[2, p.130]

Bruce Hoglund has also posted commentary on why the MSR program was abandoned on his website in a 2010 essay titled "Why the Molten Salt Reactor (MSR) Was Not Developed by the USA". [3]

1.2.3 Involvement in Generation IV

A resurgence in interest in MSRs is seen, starting in the early 2000s. One paper written in this third period of development was David LeBlanc's 2010 paper *Molten salt reactors: A new beginning for an old idea* [4] which concluded the prior work on MSRs had reduced research and development needs to *"far less than many may imagine"*.

Since then, the molten salt reactor technology has been under active development, and it is being actively considered for deployment within the Generation-IV nuclear power program. [5]

1.3   Xenon 135

1.3.1   History

The following history is summarized from the account by Richard Rhodes [6].

The importance of Xe-135 in the operation of nuclear reactors was discovered early in the history of the field. Although the earliest, low power, reactors did not encounter any operating experience with xenon poisoning, the problem revealed itself when the 250 MW_{th} Hanford B reactor began operation in 1945. The reactor achieved initial criticality in the Morning of September 26, 1945 and operated normally throughout the work day. In the evening, after the project

scientists had gone home, the reactor power level began dropping. Operators began removing control rods to attempt to raise reactor power, however, by early morning on the 27th, the reactor had effectively shut down.

The next day, the reactor began to mysteriously regain power, however by the evening of that day the reactor shut down again. Scientists, at the time, were aware of the possibility of fission product poisoning, but were unsure as to how exactly it would occur. Project physicist John A. Wheeler searched the table of isotopes and after numerous calculations, finally concluded that it was the chain of I-135 and Xe-135 explained the observed *breathing* behavior of the reactor.

General Groves, the military command of the Manhattan project was informed of the issue by Author Compton, and reportedly took the news *acidly*. Compton was reported to have apologized to Groves for a *"fundamentally new discovery regarding the neutron properties of matter"*.

1.3.2 Evolution of Xe-135

The production and decay of Xe-135 is typically modeled with the production and decay of Te-135 and I-135, shown in Figure 1.3. Xe-135 (8) enters the system either direction through fission production (7) or from the decay of I-135 (6). Xe-135 exists the system either when it beta decays (12) to Cs-135 with a characteristic 9.1 h half life or it absorbs a neutron (9) and transmutes into Xe-136. I-135 (5) is a progenitor of Xe-135 and beta decays into it with a characteristic half life of 6.57 h. I-135 can either be produced directly from fission (4), or from the decay of Te-135 (2). Te-135 is produced by fission (1) and has a characteristic half life (3) of 19 s. During the early modeling efforts of xenon in the MSRE, Te-135 hadn't been separated from I-135 yet, and many reports either omit its existence or have the wrong half life for Te-135. The

(1)Te-135 Fission Production (4) I-135 Fission Production (7) Xe-135 Fission Production

(2) Te-135 → (3)$t_{1/2} = 19$ s → (5) I-135 → (6) $t_{1/2} = 6.57$ h → (8) Xe-135 → (11) $t_{1/2} = 9.1$ h → (12) Cs-135

(9) N^0 Abs.

(10) Xe-136
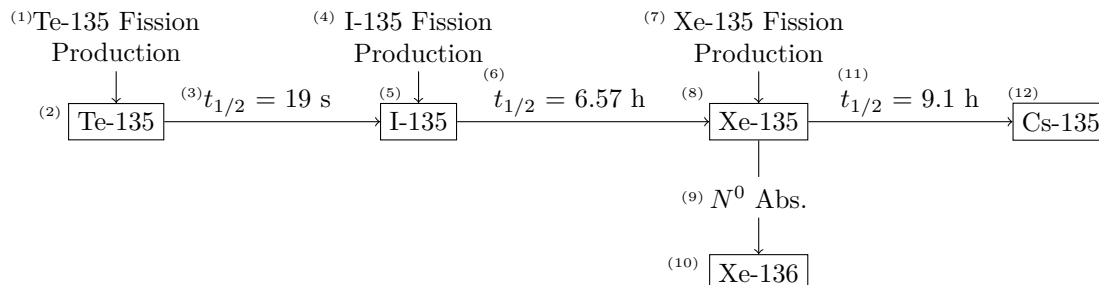
Figure 1.3: Illustration of xenon decay chain

majority of Xe-135 in the system comes from the decay of I-135 rather than direct fission production since the fission yields for Te-135 and I-135 are about an order of magnitude greater than that for Xe-135.

1.3.3 Properties of Xe-135

Xe-135 is unusual in that it has an extremely large thermal neutron absorption cross section — usually cited as around 2.6 Mb. This is because neutron capture in a Xe-135 nucleus will give the nucleus 82 (a so called *magic number*) neutrons which will complete its neutron shell.

Due to the quantum mechanical and electronic properties of atomic xenon, the question *"What is the size of a xenon atom?"* is a question in of itself. That is to say, since a xenon atom is not a solid physical object, what is it that we mean when we say *"the size of a xenon atom"*? This sentiment is reflected in Pau, Berg, and McMillan's 1990 paper on the application of Stoke's law to ions in aqueous solution,

> "One of the most difficult questions involved in the transition from
> a continuum medium to the case of real solvent molecules of size

Type	Radius [Å]	Reference
Covalent Radius	1.36	[9, p. 9-58]
van der Waal's Radius	2.16	[ibid.]
Lennard-Jones Collision Radius	2.02	[10, p.24]
Grimes, Blander, Watson	2.18	[8]
Kinetic Theory	1.75	[11, p. 249]

Table 1.1: Atomic Radii of Xenon

comparable to the atomic dimensions of the mobile ion is unit is the meaning to be attached to the particle 'radius'." [7]

Table 1.3.3 lists some radii of xenon from various sources. Blander, Grimes, Smith and Watson report the radii of rare gas atoms in a solid would be a lower limit of a hole created by a gas atom in a molten salt. [8]

1.3.4 Poisoning Effects in Nuclear Reactors

When Xe-135 accumulates in a nuclear reactor, it is said to *poison* the reactor. When a nuclear reactor undergoes a power maneuver in which power is lowered, the quantity of xenon in a reactor follows a characteristic curve in which the quantity of Xe-135 in the reactor temporarily increases beyond its steady state value for a period of several hours before decaying away. The period in time in which the xenon is above its steady state value is known as the *iodine pit* [3]. If the height of this iodine pit is large enough, the reactor will *poison out.* since the reactivity control mechanisms cannot compensate for the negative reactivity introduced by the xenon.

1.4 Xenon in Molten Salt Reactors

This section provides a brief overview of the behavior of Xenon in MSRs. For a full review, see [12].

---

[3]A pit rather than a hill since the xenon introduces negative reactivity. When the reactivity contribution from Xe-135 is plotted with respect to time, it produces a characteristic *pit* shape.
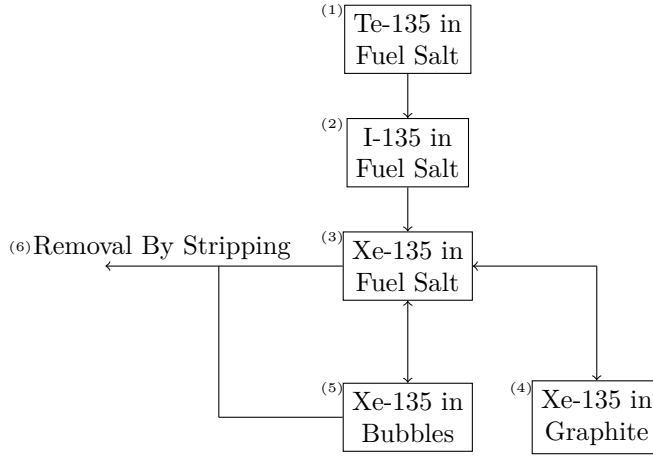
Figure 1.4: Overview of xenon migration in an MSR

1.4.1   The Overall Theory of Xenon in Molten Salt Reactors

Figure 1.4 illustrates the overall behavior of xenon in an MSR. As described in Subsection 1.3.2, xenon enters the system in the fuel salt through the Te-I-Xe (135) decay chain — (1), (2), and (3). Xenon enters the system in the fuel salt (3) and is then free to migrate between the fuel salt and the bubbles[4], (5), or the fuel salt and the graphite, (4). Some early work, ORNL-TM-3464 [13], hypothesized bubbles may be able to ingress indirectly into the graphite, but we think this unlikely considering during normal operation, the graphite is hotter than the fuel salt (and therefore, presumably, the bubbles as well). Xenon in either the bubbles or the fuel salt is then removed by the xenon stripper, (6).

According to Henry's law, there is a preference for dissolved gas species to favour the gas phase over the liquid phase, and therefore, a minority of xenon will be found dissolved in the fuel salt itself. Furthermore, the mass transfer coefficient on the bubbles is significantly larger than that of the graphite and therefore, most of the xenon will be found in the circulating voids.

---

[4]The bubbles are also called the *circulating voids* elsewhere in the literature.

1.4.2 The In Solution Assumption

One of the more interesting aspects of the Xe-135 decay chain (shown in Figure 1.3) is that Xe-135 is a noble gas at MSR operational temperatures whereas Te-135 and I-135 are either solids or liquids. We therefore use the *in solution assumption* in our analysis of MSR xenon behavior. The in solution assumption states that Te-135 and I-135 remain dissolved in the fuel salt whereas the Xe-135 is free to migrate. Experimental evidence in the MSRE indicates this assumption is valid and is discussed in further detail in ORNL-TM-3464 [13].

1.4.3 The Ideal Dilute Solution Assumption and Henry's Law

The mass transfer equations used in MSR xenon theory make ample use of Henry's law to relate the liquid and gas phase xenon concentrations. Formally, Henry's law is defined as,

$$\lim_{C_i \to 0} H_i = \frac{C_i}{p_i},$$

(1.8)

where C_i is the concentration of species i in the liquid phase and p_i is the partial pressure of species i in the gas phase. Note, Henry's law is defined for when the concentration of the dissolved species in the liquid phase approaches zero, which is the definition of an *ideal dilute solution*. Therefore, the fuel salt in MSR xenon analysis is assumed to act as an ideal dilute solution so as to allow for the application of Henry's law.

1.4.4 Migration Into Graphite

The graphite moderator in many MSR designs, including the MSRE, is not a solid block of graphite, but, rather, is a porous matrix of compressed and bound graphite particles. The space between these particles is called the *pore space* or *void space* and occupied about 10% of the volume of the MSRE graphite. The

pores of the MSRE graphite were sufficiently small ($1\,\mu\text{m}$ to $3\,\mu\text{m}$, see ORNL-4148 [14]) that fuel salt could not penetrate into the pore space. Since xenon is a gas, it is assumed to be able to come out of solution and migrate into the graphite pore space.

Since fuel salt does not penetrate into the graphite, there is no xenon nor xenon progenitor production within the graphite, and all xenon within the graphite originated from the fuel salt. The xenon, however, is still subject to decay and burnout processes.

The migration of xenon into the graphite stringer is modeled by the expression,

$$J = k_m \left(C_L - \frac{HRT}{\epsilon} C_{Gr} \right),\tag{1.9}$$

which is derived from Fick's law for Porous media.

Although some work, such as ORNL-TM-3464 [13], has used a lumped volume approach to modeling mass transfer to graphite stringers, this model uses a transient reaction diffusion equation in cylindrical coordinates,

$$\frac{\partial C_{Xe}}{\partial t} = \frac{D_g}{\epsilon} \left(\frac{\partial^2 C_{Xe}}{\partial r^2} + \frac{1}{r} \frac{\partial C_{Xe}}{\partial r} \right) - \left(\sigma_a^{Xe} \phi + \lambda_{Xe} \right) C_{Xe},\tag{1.10}$$

where ϕ is the neutron flux within the graphite stringer itself (note, the graphite neutron flux is different than the fuel salt neutron flux).

1.4.5 Migration into Bubbles

Migration of xenon into the bubbles is modeled by,

$$J = k_m (C_L - HRTC_B).\tag{1.11}$$

The bubbles are assumed to be sufficiently small and diffusive and advective processes within the bubbles sufficiently fast that they can be modeled with a

lumped volume approach.

The bubble surface area is calculated through a *reference diameter* in which the total gas volume in the reactor is divided into a number of spherical bubbles with diameters equal to the reference diameter and the mass transfer area found by determining the total surface area for all of those bubbles.

1.4.6   Xenon Stripping

The xenon stripper removes xenon by spraying fuel salt through numerous small holes on the xenon stripper into a pool of fuel salt. The increased surface area of the xenon stripper allows the fuel salt to contact the cover gas and subsequently expel the xenon through mass transfer.

The xenon stripper operation is characterized by three variables, the volumetric flow rate, $\dot{Q}$, of the stripper, the bubble stripping efficiency, η_B, and the fuel salt stripping efficiency, η_{FS}.

The rate of removal of xenon from the fuel salt is calculated through,

$$\dot{N}_{Xe}^{FS.\ Strpr.} = \eta_{FS} C_{Xe}^{FS} \dot{Q}^{Strpr.}, \tag{1.12}$$

and the rate of removal of xenon from the bubble phase is calculated through,

$$\dot{N}_{Xe}^{B.Strpr.} = \eta_B C_B V_B^1 \dot{Q}^{Strpr.} C_{Xe}^B. \tag{1.13}$$

1.5   Summary and Chapter Conclusion

This chapter has attempted to lay out a minimal primer on the background theory required to understand the work. A brief primer on reactor theory is provided for the sake of completion and to ensure the reader and the author have

a common frame of reference for the forthcoming discussion[5] Molten salt reactors are described at a conceptual level and previous reactors, both experimental and constructed, have been reviewed. The history, evolution, and properties of Xe-135 have been discussed along with a brief explanation on how it effects nuclear reactors.

Finally, the behavior of xenon in MSRs has been described. This is, to the best of our knowledge, the first primer on MSR xenon behavior written since ORNL-4541 [15] in 1971 and includes several aspects not discussed in ORNL-4541. The in solution assumption for tellurium and iodine is described along with the ideal dilute solution assumption. Migration of xenon into graphite and the circulating voids is also discussed. The action of the xenon stripper is described.

---

[5]It also seems *right* to start a nuclear engineering thesis at the level of atoms.

CHAPTER 2

Model Description

2.1 Serpent Model

The macroscopic fission cross section was a parameter of the MSRE that was not found elsewhere in literature. Therefore, it was generated using the Serpent 2 Reactor physics code [16]. The model is shown in Figure 2.1 and was developed by a University of Tennessee student, Gavin Ridley, using available reference data from ORNL-TM-0728 [17].
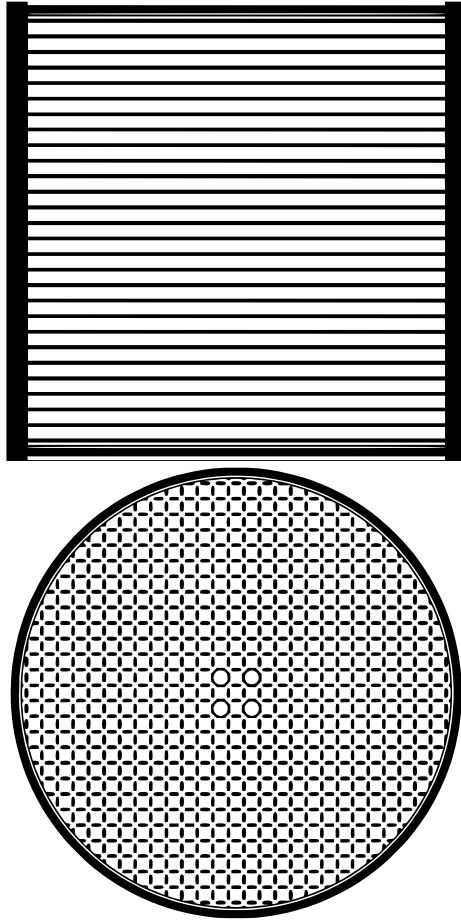
Figure 2.1: Visualization of Serpent MSRE model; top and side view, cut through the center plane.

Benchmarking of the Serpent model was done by modeling control rods in the reactor and comparing the calculated rod worths to measurements reported in ORNL-TM-0728 [17], page 101. Table 2.1 shows the results of this bench marking. The macroscopic fission cross section was found to be $0.15\,[\mathrm{m}^{-1}]$.

No. Rods Inserted	k_{eff}	Error [$\pm$pcm]	Calculated Worth [pcm]	Reported Worth [pcm]
0	1.04735	34		
1	1.0169	31	3045	2.8×10^3
2	0.99323	35	5412	5.0×10^3
3	0.97324	39	7411	6.7×10^3

Table 2.1: Results of Serpent 2 control rod worth simulations with data from ORNL-TM-0728 with 35% ^{235}U fuel.

2.2 Progenitor Subsystem
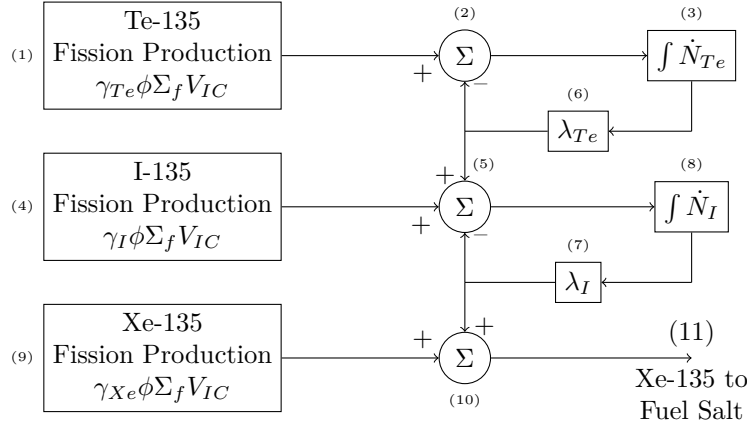
Figure 2.2: Illustration of progenitor subsystem

An illustration of the xenon progenitor subsystem is shown in Figure 2.2. The progenitors system implements the *in solution assumption* in which Te-135 and I-135 are both assumed to remain in solution as a homogeneous mixture. The subsystem tracks the total quantity of Te-135 and I-135 in the fuel salt

Isotope	Fission Yield
Te-135	3.22×10^{-2}
I-135	2.94×10^{-2}
Xe-135	2.57×10^{-3}

All yields from [18].

Table 2.2: Fission product yields for U-235 used in the dynamic model

rather than its concentration.

The isotopes, Te-135, I-135, and Xe-135 are all produced by fission in blocks (1), (4), and (8) respectively. Production of an isotope, i, is governed by an equation of the form,

$$\dot{N}_i = \gamma_i \phi \Sigma_f V_{IC}, \tag{2.1}$$

where γ_i is the fission yield for isotope i, ϕ is the neutron flux, Σ_f is the macroscopic fission cross section, and V_{IC} is the in-core volume. The fission yields used assume the fissioning isotope was pure U-235. The fission yields for the poison isotopes are shown in Table 2.2. The neutron flux, ϕ, at full power, was taken to be the average thermal neutron flux of $1.5 \times 10^{17}\,\mathrm{m}^{-1}\,\mathrm{s}^{-2}$ described in ORNL-TM-0728 [17, p. 101]. The macroscopic fission cross section, Σ_f, was a one group cross section generated using the Serpent model described in Section 2.1. The in-core volume, V_{IC} was $1.29\,\mathrm{m}^3$, and was calculated by summing the *"core"*, *"lower head"*, and *"upper head"* volumes described in ORNL-TM-0728 [17], page 102. (More details on the volumes used in the model are provided in Section 2.5) The rationale behind including the upper and lower head volumes in the model's in-core volume is that the *"core"* volume described in ORNL-TM-0728 is taken to be the fuel salt volume between the upper and lower planes of the graphite stringers (i.e. that which is inside the fuel channels only) whereas it is assumed the neutron flux in the upper and lower heads (plenum) is non-negligible and should be factored into any production calculations.

The quantity of Te-135 and I-135 in the system is tracked by the integrators

Isotope	Half Life	Decay Constant (s^{-1})
Te-135	19 s	3.65×10^{-2}
I-135	6.57 h	2.9306×10^{-5}
Xe-135	9.2 h	2.0924×10^{-5}

Data can be found in numerous sources such as [19].

Table 2.3: Half life data used in the dynamic model

shown in blocks (3) and (8) respectively. The decay of isotope, i, is accounted for by using the radioactive decay law,

$$\dot{N}_i = -\lambda_i N_i, \tag{2.2}$$

where N_i is the quantity of isotope i and the λ_i is its decay constant which can be found from the half life using $\lambda_i = log(2)/t^i_{1/2}$. This is implemented in blocks (6) and (7) respectively. The half life data used in the model is shown in Table 2.2.

The rate of accumulation of a poison isotope is the difference between the fission production rate and its decay rate. This is implemented in blocks (2) and (5) for Te-135 and I-135 respectively. Decay of Xe-135 is accounted for by the fuel salt, graphite, and bubble models respectively, and therefore is not implemented in the progenitor subsystem. The transmutation of Te-135 into I-135 is accounted for by adding the rate from block (6) into block (5). Likewise, the transmutation of I-135 into Xe-135 is accounted for by feeding the output of block (7) into block (10). Finally, the output of the system, (11), is used as an input into the fuel salt subsystem, indicted by block (1) in Figure 2.3.

2.3   Fuel Salt Subsystem

The fuel salt subsystem is illustrated in Figure 2.3. The subsystem assumes the fuel salt circulates sufficiently fast for the entire fuel salt to be treated as a well
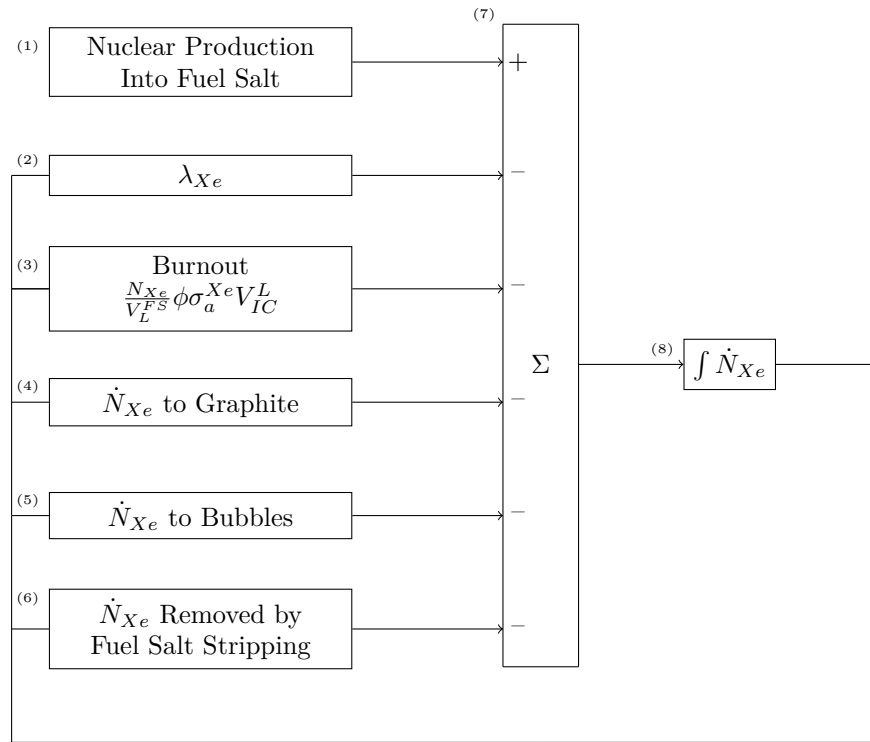
Figure 2.3: Illustration of fuel salt subsystem

mixed solution.

Nuclear processes that affect the evolution of Xe-135 are implemented in blocks (1), (2), and (3). The nuclear production of Xe-135 from the progenitor subsystem, which was shown in Figure 2.2, is accounted for in block (1). Decay of Xe-135 in the fuel salt is accounted for by block (2) which implements Equation 2.1. The magnitude of the decay constant can be found in Table 2.2. Nuclear transmutation of Xe-135 into Xe-136 (burnout) is accounted with block (3) which implements,

$$\frac{N_{Xe}}{V_L^{FS}}\phi\sigma_a^{Xe}V_L^{IC}, \tag{2.3}$$

The volume normalization constant is taken to be the entire liquid contents of the fuel salt, V_L^{FS}, whereas the production volume is taken to be the in core liquid volume, V_L^{IC}

For the burnout block, (3), the neutron flux, ϕ, at full power, was taken to be the average thermal neutron flux of $1.5 \times 10^{17}\,\mathrm{m^{-1}\,s^{-2}}$ described in ORNL-TM-0728 [17, p. 101]. The microscopic neutron absorption cross section, σ_a^{Xe}, was $1.18\,\mathrm{Mb}$, taken from ORNL-4069 [20, p. 42].

The next three blocks, (4), (5), and (6), describe mass transfer processes in the reactor. Block (4) accounts for migration into the graphite subsystem, described in Section 2.6. Block (5) accounts for migration into the circulating voids (bubbles) and is described in Section 2.7. Finally, block (6) accounts for removal of xenon from the fuel salt (but not the bubbles — described later) and is described in Section 2.8.

All of these source and sink terms (blocks (1) through (6)) are summed by block (6) which is fed into an integrator at block (8) which tracks the quantity of Xe-135 dissolved in the liquid phase of the fuel salt.

2.4 Thermophysical Properties and Dimensionless Numbers

2.4.1 Material Properties

Each of the graphite and bubble nodes used in the model calculates its thermophysical properties and dimensionless numbers locally. This subsystem is diagrammed in Figure 2.4. The magnitude of the thermophysical properties and the Schmidt number is plotted in Figure 2.5. For the proceeding discussion, numbers enclosed by parentheses are referring to Figure 2.4 and statements about plots are referring to Figure 2.5.
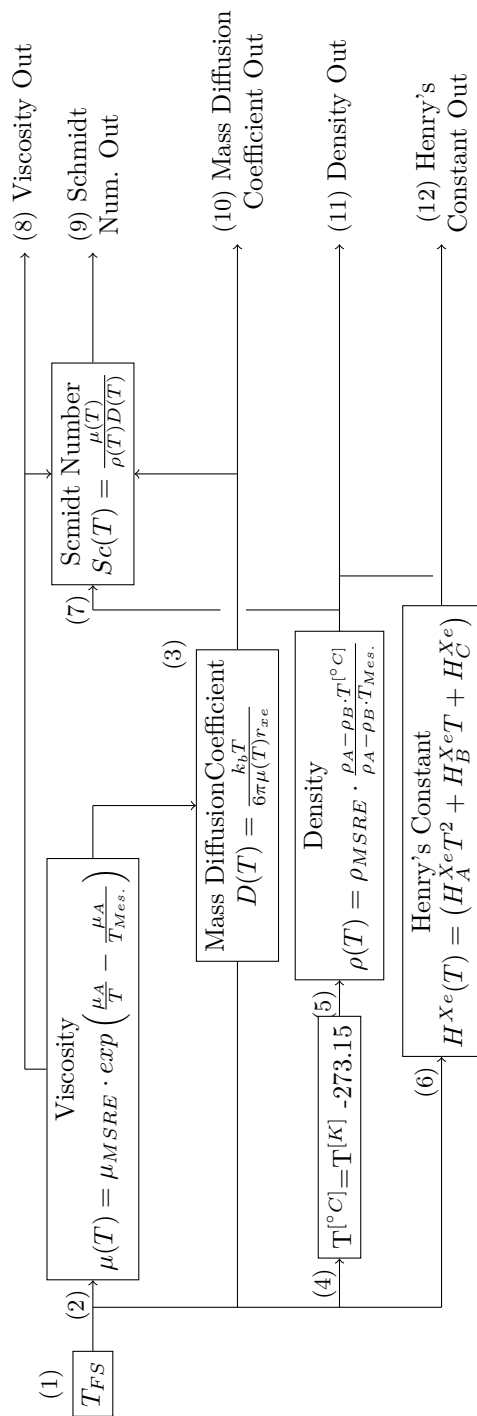
Figure 2.4: Diagram of subsystem that calculates thermophysical properties and dimensionless numbers

The diagram contains the following labeled elements:

(1) T_{FS}

(2) Viscosity
$$\mu(T) = \mu_{MSRE} \cdot exp\left(\frac{\mu_A}{T} - \frac{\mu_A}{T_{Mes.}}\right)$$

(3) Mass Diffusion Coefficient
$$D(T) = \frac{k_b T}{6\pi\mu(T)r_{xe}}$$

(4) $T^{[°C]} = T^{[K]} - 273.15$ (5)

Density
$$\rho(T) = \rho_{MSRE} \cdot \frac{\rho_A - \rho_B \cdot T^{[°C]}}{\rho_A - \rho_B \cdot T_{Mes.}}$$

(6) Henry's Constant
$$H^{Xe}(T) = (H_A^{Xe}T^2 + H_B^{Xe}T + H_C^{Xe})$$

(7) Scmidt Number
$$Sc(T) = \frac{\mu(T)}{\rho(T)D(T)}$$

(8) Viscosity Out

(9) Schmidt Num. Out

(10) Mass Diffusion Coefficient Out

(11) Density Out

(12) Henry's Constant Out

The thermophysical property subsystem has three inputs inputs:

- T_{FS}, the local fuel salt temperature (1);

- U, the local fuel salt velocity (14);

- L, the local characteristic hydraulic length for a given node.

The outputs for the subsystem are:

- μ, fuel salt viscosity (8);

- Sc, the Schmidt number[1] (9);

- D, the mass diffusion coefficient (10);

- ρ, the density of the fuel salt (11);

- (12), the Henry's constant, defined in terms of dissolved concentration and partial pressure — $H_i^{CP} = \frac{C_i}{p_i}$ — (12);

- The local Reynolds number.

Each node in the lumped volume subsystem (Section 2.5) has has its own instance of the thermophysical property subsystem.

The variation of MSRE fuel salt density and viscosity with temperature was not found in the literature. ORNL-TM-2316 [21], however, does provide several temperature dependent correlations for density, on page 8, and viscosity, on page 28, for several potential MSRE fuel salts that were under consideration. Furthermore, ORNL-TM-0728 [17], page 8, also provides the density and viscosity for fuel salt used in the MSRE at 1200°F (649 °C). Therefore, in order to provide some sort of temperature dependence of the fuel salt used in the model, a *temperature scaling factor* was generated. The final density/viscosity

---

[1]The ratio of momentum to mass diffusivity

Variation of Thermophysical
Properties With Temperature
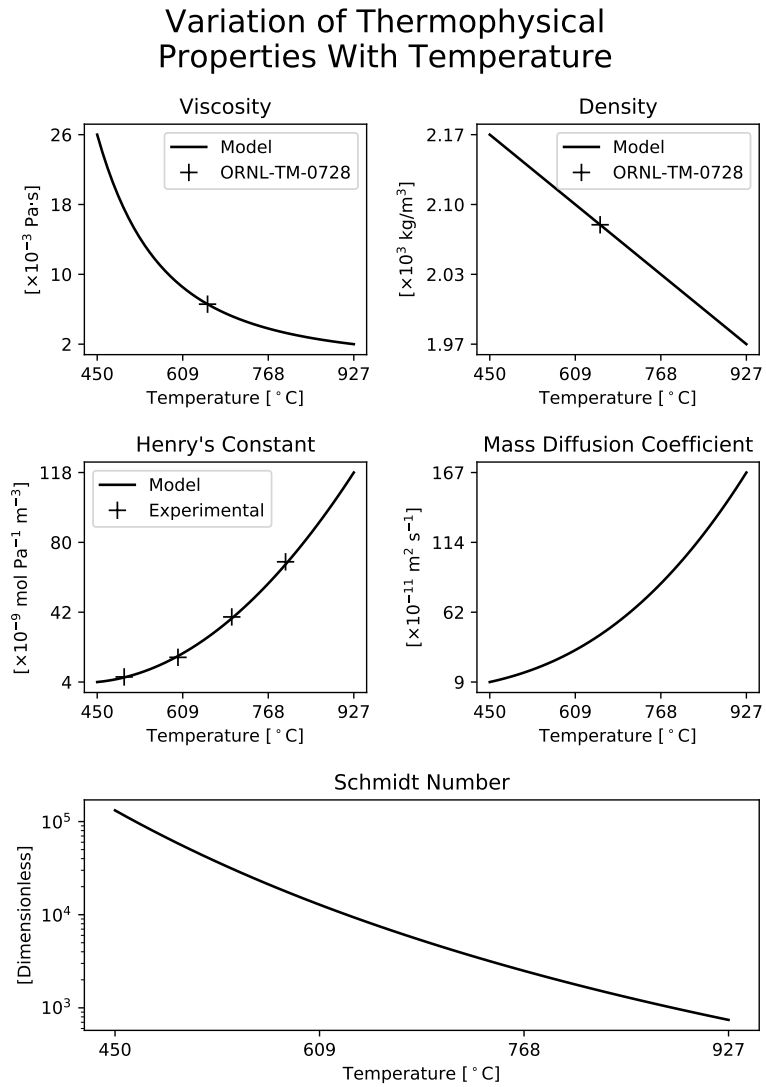
Figure 2.5: Plots thermophysical properties used in the dynamic model

was derived at by multiplying the reported density/viscosity 1200° by the scaling factor. The scaling factor was derived by evaluating the density/viscosity of fuel salt F1 in ORNL-TM-2316 at the model's fuel salt temperature and dividing that quantity by the density/viscosity of fuel salt F1 in ORNL-2316 at 1200°F:

$$\rho \text{ Scaling Factor} = \frac{\rho(T)}{\rho(T_{Mes.})}, \tag{2.4}$$

$$\mu \text{ Scaling Factor} = \frac{\mu(T)}{\mu(T_{Mes.})}, \tag{2.5}$$

where $T_{Mes.}$ is the temperature at which the MSRE fuel salt had its density and viscosity measured (1200°F). Therefore, the final output density/viscosity is given by an expression of the form

$$\rho(T) = \rho_{MSRE} \cdot (\rho \text{ Scaling Factor}), \tag{2.6}$$

or,

$$\mu(T) = \mu_{MSRE} \cdot (\mu \text{ Scaling Factor}), \tag{2.7}$$

respectively.

Fuel salt F1 was used from ORNL-TM-2316 because it as judged to have the closest chemical composition to the fuel salt used in the MSRE. The *"highly enriched"* fuel salt variant was used as a source for the base density/viscosity data.

The viscosity correlation was presented in ORNL-TM-2316 in the form,

$$\mu(T) = \mu_K \cdot exp\left(\frac{\mu_A}{T}\right), \tag{2.8}$$

and the density correlation was presented in the form,

$$\rho(T) = \rho_A - \rho_B T. \tag{2.9}$$

The constants used in equations 2.8 and 2.9 are presented in Table 2.4.

Constant	Value
ρ_A	$3.62\,\mathrm{g\,cm^{-3}}$
ρ_B	$6.6 \times 10^{-4}\,\mathrm{g\,cm^{-3}\,^\circ C^{-1}}$
μ_K	8.4×10^{-2} cP
μ_A	6.6×10^{-4} K

Table 2.4: Magnitude of parameters used in viscosity and density correlations

Note, the temperature in Equation 2.8 is expected to be in Kelvin whereas the temperature in Equation 2.9 is expected to be in degrees Celsius. The dynamic model natively stores the temperature in Kelvin, so unit conversion for the density calculation in block (5) is handled by block (4).

The viscosity is calculated by block (2) which implements the equation,

$$\mu(T) = \mu_{MSRE} \cdot exp\left(\frac{\mu_A}{T} - \frac{\mu_A}{T_{Mes.}}\right). \tag{2.10}$$

The multiplicative constant, μ_K, shown in Equation 2.8 is removed by simplification, and the entire equation is transformed from the evaluation of two exponential to a single exponential by the well known rule that states the quotient of two exponential function is equal to the exponential of the difference of the arguments to those original exponentials. Note, since the correlation implemented by Equation 2.8 returns a value in centipoise, this must be converted to a pascal second, which is congruent with the model's native SI units, through a multiplication operation that is not depicted.

The density calculation, implemented in block (5), takes as its input parameter the temperature in degrees Celsius and outputs the local fuel salt density

in kilograms per cubic meter, and this is depicted by block (4).

The top row of Figure 2.5 shows the dependence of both the viscosity and density on temperature. The measured value of the MSRE fuel salt, reported on page 8 of ORNL-TM-0728 [17], is denoted by a "+" sign on these plots. The data is plotted from $450\,°C$ (MSRE fuel salt liquidus temperature is $448\,°C$) to $927\,°C$ ($1200\,K$). Over this temperature range, comparing the low temperature value to the high temperature value, the viscosity decreases by a factor of 13 whereas the density decreases by about 1%. It is therefore foreseeable that establishing an accurate temperature dependence for viscosity is far more important than establishing an accurate temperature dependence for density.

Next is block (6), the block that calculates the magnitude of Henry's constant. Again, the particular variant of Henry's constant that is calculated is the pressure-concentration (H^{CP}) variation rather than the dimensionless (H^{CC}) variation. This block implements a quadratic fitting function of the form,

$$H^{Xe} = H_A^{Xe}T^2 + H_B^{Xe}T + H_C^{Xe}, \tag{2.11}$$

to obtain the temperature dependence of Henry's constant on temperature. The constants H_a^{Xe}, H_b^{Xe}, and H_c^{Xe} are fitting parameters. The data that was fitted was obtained from experiments with FLiBe salt presented in a 1962 paper by Watson, Evans, Grimes, and Smith [22]. The raw data was presented as a dimensionless Henry's constant, so they needed to be normalized by their measurement temperature and the ideal gas constant to derive the appropriate dimensional form of the constant. The magnitudes of the fitting parameters are shown in Table 2.4.1. A plot of this fitting function along with the experimental data points from which the fitting function is derived is shown in the first column of the second row of Figure 2.5. Although a linear function could have been used to fit the data, our experience indicates a quadratic function provides a

superior fit (R-Squared value of 0.9635 for linear vs. 0.9994 for quadratic). A better fitting function would require more experimental data points at higher temperatures.

Constant	Magnitude	Unit
H_a^{Xe}	4.426×10^{-13}	$\mathrm{mol\,m^{-3}\,Pa^{-1}\,K^{-2}}$
H_b^{Xe}	-6.124×10^{-10}	$\mathrm{mol\,m^{-3}\,Pa^{-1}\,K^{-1}}$
H_c^{Xe}	2.153×10^{-7}	$\mathrm{mol\,m^{-3}\,Pa^{-1}}$

Table 2.5: Magnitudes of parameters used in the generation of Henry's constant

The mass diffusion coefficient is calculated using block (3). The block implements the Einstein-Stokes equation to calculate the mass diffusion coefficient for a diffusing spherical particle in a continuous medium,

$$D(T) = \frac{k_b T}{6\pi\mu(T)r_{Xe}}, \tag{2.12}$$

where T is the temperature of the fuel salt, in Kelvin, k_b is Boltzmann constant ($1.38 \times 10^{-23}\,\mathrm{N\,m\,K^{-1}}$), $\mu(T)$ is the viscosity of the fuel salt at temperature T, and r_{Xe} is the radius of the xenon atom diffusing in fuel salt. The radius of the diffusing atom was set to $216\,\mathrm{pm}$. The temperature evaluated viscosity is input into this block (3) from block (2), the viscosity calculation block. A plot of the mass diffusion coefficient with respect to temperature is shown in the second column of the second row of Figure 2.5. Note the clearly non-linear temperature dependence of the function; this is caused by the non-linearity of the viscosity with respect to temperature.

Finally, the non-dimensional number, the Schmidt number is calculated using blocks (7). The Schmidt number is purely a function of material parameters, and has for its inputs, viscosity, density, and the mass diffusion coefficient. A logarithmic plot of the Schmidt number with respect to temperature is shown in the last row of Figure 2.5. This plot shows that the Schmidt number decreases

by more than two orders of magnitude between the high and low temperatures plotted.

2.4.2 The Reynolds Number

The method by which the Reynolds number is calculated is dependent on the type of node the Reynolds number is being calculated in. There are three types of nodes:

- Cylindrical piping sections

- No correlation available

The subsystems to calculate each of these Reynolds numbers is shown on Figure 2.6.

The Reynolds numbers are calculated with blocks (8) and (9). All blocks take in that node's fuel salt temperature, block (1) as a temperature argument. The outputs to the subsystem are the pipe Reynolds number (10) and the scaled Reynolds number (11). Note, that for a given node, only one of these Reynolds numbers is calculated and therefore signals need not necessarily be present in all lines. Additionally, all methods of calculation also take in the viscosity, μ, and the density, ρ, through blocks (4) and (5) respectively and these values are provided by the thermophysical property system described previously..

The block that calculates the pipe Reynolds number, takes in the fuel salt flow velocity, u, through block (3) and the hydraulic diameter of the cylindrical diameter, L, through block (2).

The scaled Reynolds number block, block (11), scales a predetermined Reynolds number, Re_0, by the ratio of the Reynolds number evaluated at temperature T, and the Reynolds number evaluated at some nominal temperature, $T_{Mes.}$. The predetermined Reynolds number is supplied by block (6) and the nominal
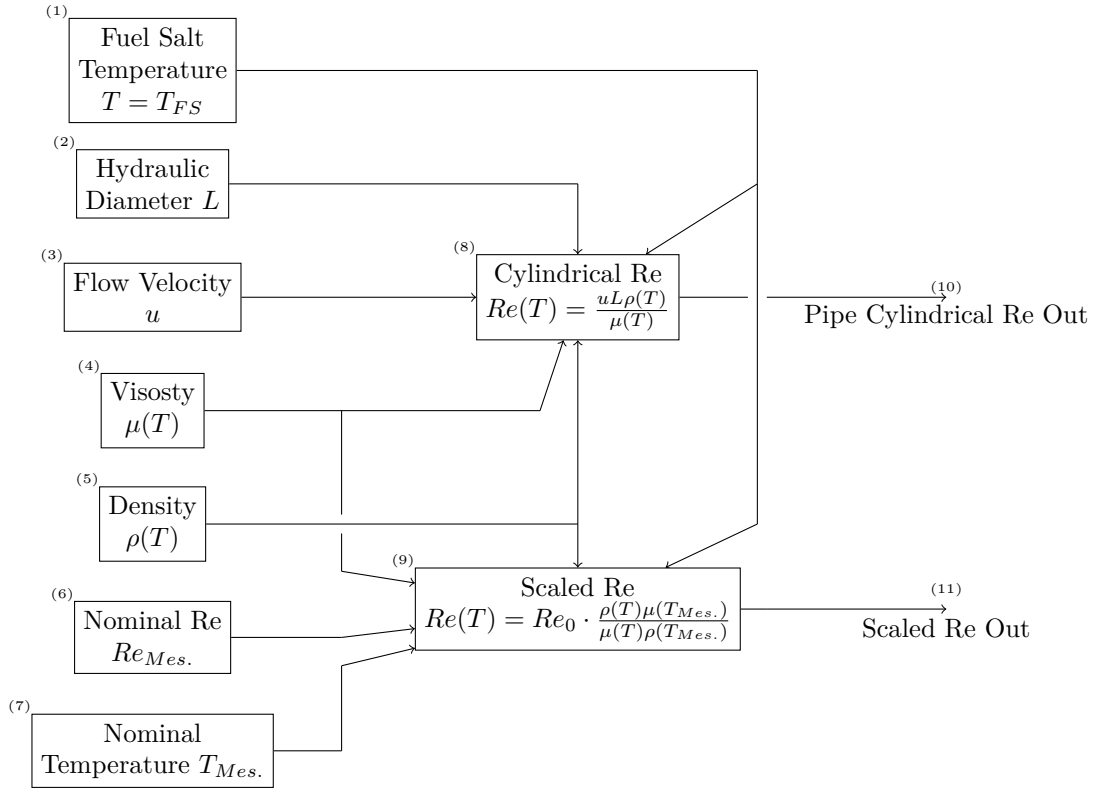
Figure 2.6: Subsystem to calculate the Reynolds number for a node

temperature is supplied by block (7). The geometry and the flow velocity are assumed to be the same in both the nominal and perturbed temperature cases, and therefore the flow velocity, u, and hydraulic diameter, L, terms cancel out, and the calculation is able to be preformed without them.

Finally, the fuel pump Reynolds number is not calculated since it is not directly used in any calculations.[2]

2.5 The Lumped Volume Subsystem

The bubble model used in the dynamic model is illustrated with Figure 2.7. The parameters used in the bubble model are shown on Table 2.8. The fourth column in this table describes the method, pipe or scaling, by which the Reynolds number is calculated in that node, and these methods are described in Section 2.4.2. The fuel salt flow path for the bubble model is illustrated with Figure 2.8.

Regions G_1, G_2, G_3, and G_4 are graphite fuel channel regions inside the core. the region numbering corresponds to the region numbers on page 14 of ORNL-TM-0378 [24]. Note, the graphite regions are somewhat specialized in that they also posses a property which describes the number of fuel channels within that region. The distribution of these fuel channels is described in Table 2.6. Additionally, each fuel channel is 1.6 m high (see ORNL-4069 [20]page 6) and has an equivalent cylindrical radius of 0.79 cm (see ORNL-4069 [20]page 65) and it is from these measurements and the number of fuel channels in a given region that mass transfer area from the to fuel salt to the graphite is calculated.

LH and UH are the lower and upper heads described on pages 96 and 103 of ORNL-TM-0728 [17]. P_{100}, P_{101}, and P_{102} correspond to lines 100, 101, and 102, described on page 173 of ORNL-TM-0728 [ibid.]. FP is the fuel pump and pump bowel described on page 12 of the same report. Finally, HX is the heat

---

[2]However, it could be through a *stirred* Reynolds number — see [23].

Region #	Number of Channels
1	12
2	940
3	108
4	78

Data from ORNL-TM-0378 [24, p. 14]

Table 2.6: Number of fuel channels for each graphite region

exchanger described on page 14 of the same report.

Volume and residency time data for all regions except the graphite regions, G_i, were taken from page 101 of ORNL-TM-0728 [17]. Volumes for the graphite regions were calculated by multiplying the total core volume, from page 101 of ORNL-TM-0728 [17], by the fraction of the total fuel channels occupying that region, from page 14 of ORNL-TM-0378 [24]. ($N_i/N_{Tot.}$). Fuel salt velocities for the graphite regions were also taken from page 14 of ORNL-TM-0378. The hydraulic diameter for the graphite regions was taken from page 65 of ORNL-4069 [20]. The residence time for each graphite region was found by dividing the fuel salt velocity in that region by the length of the fuel channel ($1.6\,\mathrm{m}$ according to page 80 of ORNL-TM-0728 [17]).

Reynolds numbers for each node were calculated according to the *pipe* or *scaling* method described in Section 2.4.2.

Precise magnitudes of the Reynolds numbers for the upper and lower heads was not found. Furthermore, the presence of *"swirl vanes"* or other equipment complicates the calculation of the Reynolds number due to (1) uncertainty on how the characteristic length should be calculated in the lower head and (2) the presence of a complex flow field due to the swirling action.

Page 26 of ORNL-TM-3229 [25] sates *"...the Reynolds number in the upper head is high for both and fuel salt and the flow is turbulent."*. The only reference to the Reynolds number of the lower head found was on page 15 of ORNL-TM-3229 [25] which stated Reynolds number of the lower head is *"high"*; it is

unclear as to how large precisely *"high"* as, however, on page 10 of the report, a *high* Reynolds number is described as over 10^4. Therefore, the base Reynolds number used for both the upper and lower heads section was 10^4.

The subsystem that manages the gas and liquid volumes for each lumped volume is illustrated in Figure 2.9. The system inputs are:

- (1) – The nominal node volume, V_0, the total *filled* volume of the node

- (2) – The nominal circulating void fraction, f_{CV}^0, which is the circulating void fraction ($\frac{V^G}{V^L+V^G}$) at the reference temperature

- (3) The reference temperature, T_{ref}, which is the nominal temperature of the node

- (4) The node temperature, T, which is the current temperature of the node.

The reference temperatures were set such that the upper head to the heat exchanger were equal to the reactor outlet temperature, the heat exchanger is the mean between inlet and outlet temperatures, and the nodes after the heat exchanger to the lower head was equal to the reactor inlet temperature. The outlet and inlet temperatures, $907.5\,\mathrm{K}$ ($1225\,°\mathrm{F}$) and $935.4\,\mathrm{K}$ ($1175\,°\mathrm{F}$) respectively, were taken from ORNL-TM-0728 [17], page 78. The heat exchanger reference temperature was set to the median between the inlet and outlet temperatures.

Each graphite region, G_1–G_4, has associated it an *effective radius* which describes the radial position of the annulus (or cylinder for the central region, G_1) of the graphite region. These radii were taken from ORNL-TM-0378 [24], p.14, and are shown in Table 2.5.

The graphite and fuel salt temperatures were digitized from the radius-dependent measurements of graphite and fuel salt temperature at steady state presented on page 42 of ORNL-TM-378 [24]. The G_1–G_4 nodes were set such

Region	Effective Radius
1	3.78" / 9.6 cm
2	24.76" / 62.89 cm
3	26.10" / 66.29 cm
4	27.58" / 70.05 cm

Table 2.7: Graphite stringer radius effective radius

that the node temperature was equal to the mean of the these digitized temperatures from the inner effective radius to the otter effective radius.

The nominal gas volume is the volume of gas at the reference temperature in the node and is calculated by node (5). The nominal gas volume has for its inputs V_0, the nominal node volume, (1), and f_{CV}^0, the nominal circulating void fraction, (2). The nominal gas volume is then simply the product of the nominal circulating void fraction, f_{CV}^0, and the nominal node volume, V_0,

$$V_0^G = f_{CV}^0 V_0. \tag{2.13}$$

The model assumes that the gas volume displaces the liquid. The nominal liquid volume, V_0^L, is calculated through block (6), and has as its inputs, (1), the nominal node volumes, V_0, and (5), the nominal gas volume. The nominal liquid volume, V_0^L is the difference between the nominal node volume and the amount of gas nominally in the node,

$$V_0^L = V_0 - V_0^G. \tag{2.14}$$

The reference density, $\rho(T_{ref})$, is the density of liquid fuel salt evaluated at the reference temperature, T_{ref}, and is implemented in block (7). The density is provided by the thermophysical properties subsystem, described in Section 2.4. The current density, $\rho(T)$, is the density of the liquid fuel salt evaluated at the current node temperature, T, and is implemented in block (8). The inputs

for these blocks are blocks (3) and (4), the reference and node temperatures respectively, T_{ref} and T.

The nominal fuel salt mass, M_{FS}^0, is the mass of the liquid fuel salt at the reference temperature, and is implemented through block (10). The nominal fuel salt mass is the product of the nominal liquid volume, V_0^L, and the density of the fuel salt at the reference temperature, $\rho(T_{ref})$.

Block (13) takes the nominal fuel salt mass, M_{FS}^0, and multiplies it by the current liquid fuel salt density, $\rho(T)$, to get the current volume of liquid that would be in the node if it were to be totally expanded by the temperature variation,

$$V_L = \rho(T)M_{FS}^0. \tag{2.15}$$

Block (9) calculates the volume of gas from the node at the current node temperature, T. It does so by applying Charle's law ($\frac{V_1}{V_2} = \frac{T_1}{T_2}$ to the nominal gas volume, V_0^G, supplied by block (5). The state from which the gas is being expanded from is the reference temperature; therefore,

$$V_G = V_0^G \frac{T}{T_{ref}}. \tag{2.16}$$

The amount of gas in the node is the current gas volume, and is output through line (19).

The amount of liquid fuel salt in the node is calculated by block (14) and is output by line (17). Block (14) subtracts the amount of gas in the node, V_G at the current node temperature, T, from the nominal node volume, V_0.

Finally, the amount of liquid displaced by the gas in the node is determined by blocks (15) and (16). block (15) sums the current liquid, V_L, and gas volumes,V_G, expanded to the current node temperature, T, to get the total volume if both the gas and liquid were expanded. Block (16) then subtracts the

value calculated by block (15) to determine the excess liquid volume out (liquid only since gas displaces liquid), and this is output through line (18).
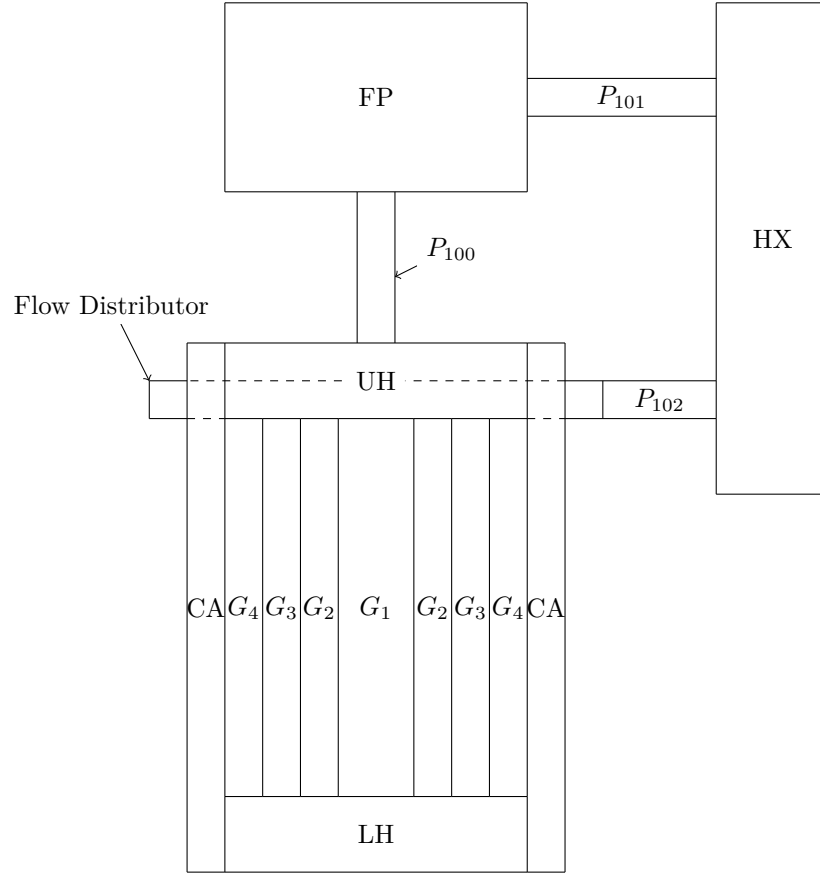
Region Code	Definition
$G_1/G_2/G_3/G_4$	Graphite Region
LH	Lower Head
UH	Upper Head
$P_{100}/P_{101}/P_{102}$	Piping Region
FP	Fuel Pump
HX	Heat Exchanger

Figure 2.7: Cross sectional illustration of bubble behavior subsystem

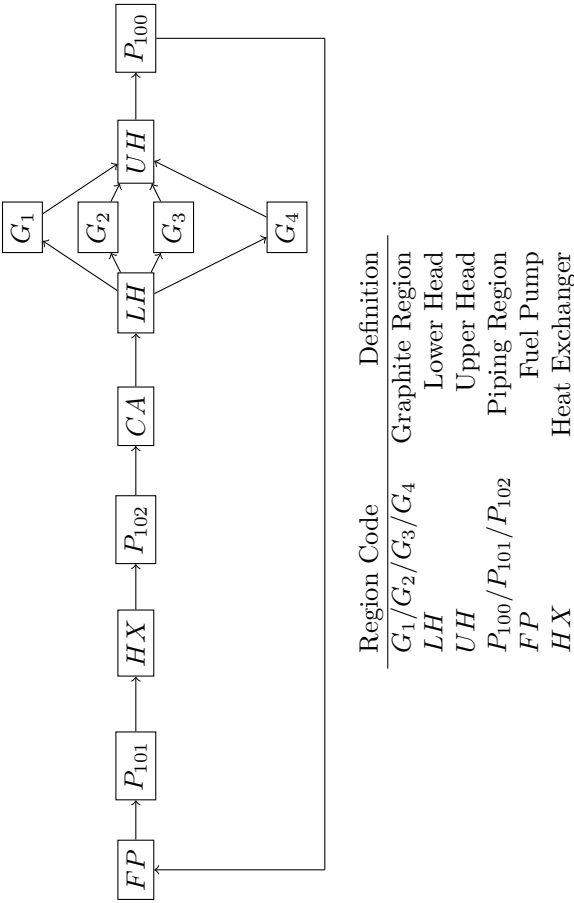| Region Code	Definition
$G_1/G_2/G_3/G_4$	Graphite Region
LH	Lower Head
UH	Upper Head
$P_{100}/P_{101}/P_{102}$	Piping Region
FP	Fuel Pump
HX	Heat Exchanger

Figure 2.8: Flow path of bubble behavior subsystem

Region	Volume (m^3)	Residence Time(s)	Reynolds Number Method	Hydraulic Diameter (cm)	Salt Velocity at 1200 GPM ($m\,s^{-1}$)	Nominal Re
G_1	7.5×10^{-3}	2.6	Pipe	1.6	0.61	
G_2	0.59	8.9	Pipe	1.6	0.18	
G_3	6.8×10^{-2}	3.6	Pipe	1.6	0.45	
G_4	4.9×10^{-2}	6.4	Pipe	1.6	0.25	
UH	0.30	3.9	Scaling			1×10^4
LH	0.28	3.8	Scaling			1×10^4
CA	0.28	3.6	Scaling			2.58×10^4
P_{100}	0.60×10^{-2}	0.8	Pipe	12.8	5.97	
P_{101}	2.3×10^{-2}	0.3	Pipe	12.8	5.97	
P_{102}	6.2×10^{-2}	0.8	Pipe	12.8	5.97	
FP	0.12	4.1	None			
HX	0.17	2.3	Pipe	1.2	4.2×10^{-2}	

Note: Re calculated from methodology described in Section 2.7.
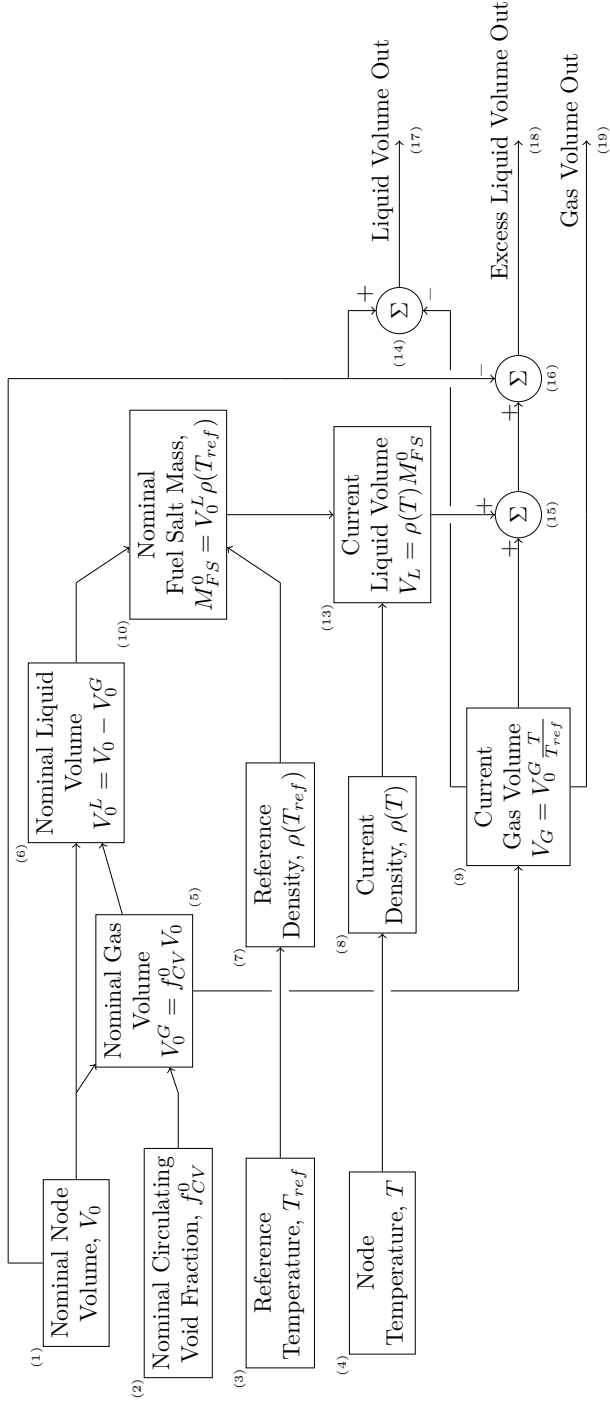
Table 2.8: Data used in Bubble Model

Figure 2.9: Illustration of lumped volume subsystem

2.6 The Graphite Subsystem

The subsystem which computes the behavior of a graphite region is shown in Figure 2.10. The inputs of the system are:

- (1), The neutron flux in the graphite, ϕ_G,

- (2), the graphite neutron flux, T_G,

- (3), the fuel salt velocity in that graphite region, U_{FS},

- (4), the quantity of Xe-135 in the fuel salt, N_{Xe}^{FS}.

As previously mentioned, each graphite region has an effective radius, which is taken from ORNL-TM-0378 [24], page 14 — the fuel salt velocity, U_{FS}, is derived from the same source.. The neutron flux, ϕ_G, for each region was determined as follows:

- ORNL-TM-0378 [24], page 23, presents neutron flux measurements as a function of radial position.

- The data presented was digitized.

- the average neutron flux across the annular radius was taken to be the neutron flux for that region.

A similar process was used to set the graphite region temperature, T_G, using the data presented on page 42 of ORNL-TM-0378 [24]. The fuel salt Xe-135 quantity, N_{Xe}^{FS}, is input from the fuel salt subsystem described in Section 2.3.

Block (4) calculates the graphite mass transfer coefficient, k_m, through a Dittus-Boelter like correlation (which was introduced by McAdams) which has been transformed into a mass transfer correlation through a heat/mass transfer analogy,

$$k_m = \frac{D}{2r_{fc}} 0.023 Re^{0.8} Sc^{0.4}. \tag{2.17}$$

The Reynolds number, Re, Schmidt Number, Sc, and the mass diff fusion coefficient, D, are all provided through the thermophysical property system described in Section 2.4.

The neutron flux, ϕ_G, graphite temperature, T_{Gr}, graphite mass transfer coefficient, k_m, and the fuel salt Xe-135 content, N_{Xe}^{FS}, are all fed into block (5), the graphite stringer model (described later), which outputs, (7), the mean Xe-135 concentration, C_{Xe}^{Gr}, and, (8), the single stringer mass flux, J. The mean Xe-135 concentration, C_{Xe}^{Gr}, is output from the subsystem directly through line (11). The single stringer mass flux, J, is multiplied by (9), the surface area of a single fuel channel, A_{FC}^1, and, (10), the number of fuel channels in the region to derive the total mass flux out, which is output through line (12).
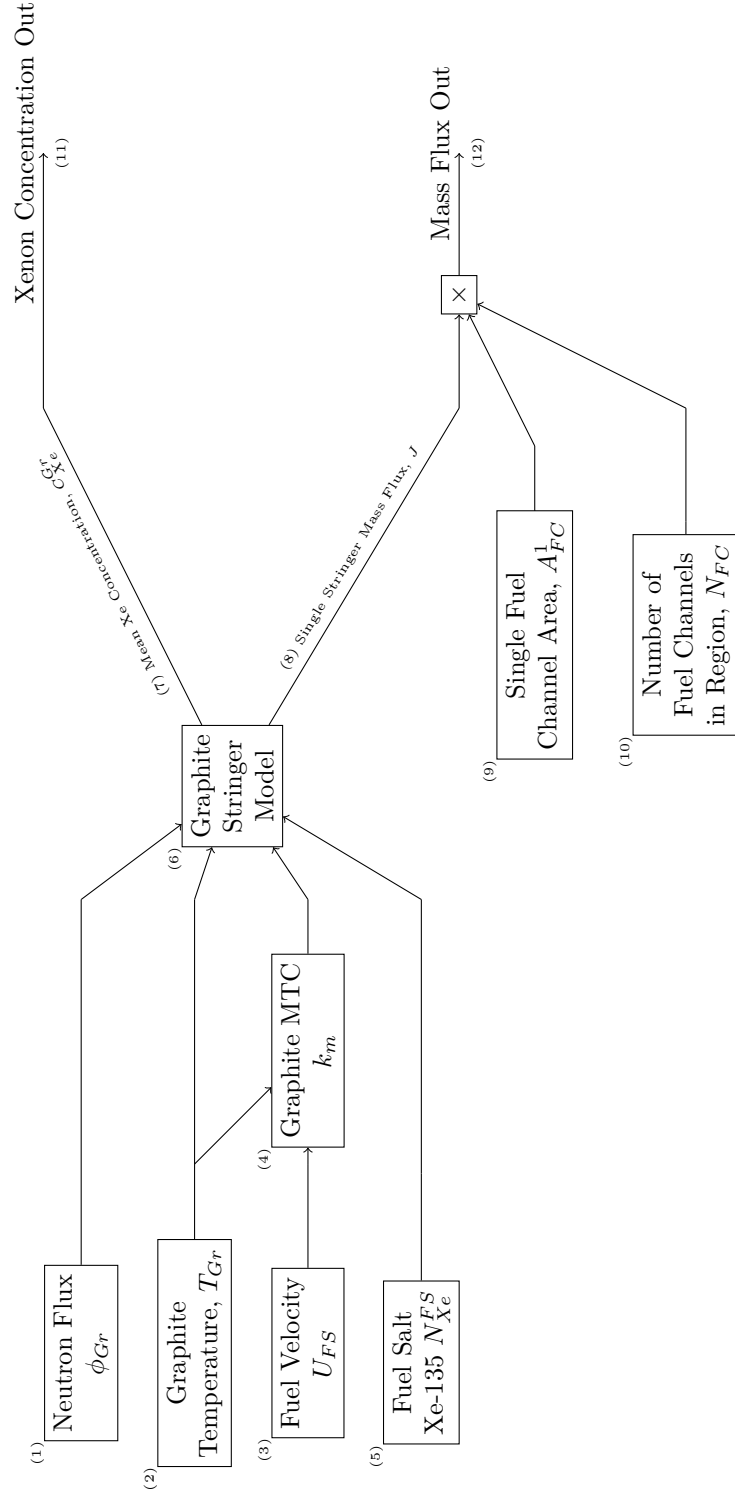
Figure 2.10: Subsystem for a graphite region

The working of the graphite stringer model, block (6) in Figure 2.10, is shown in Figure 2.11.

The first three inputs to the stringer model are,

- (1), the graphite porosity, ϵ,

- (2), the graphite mass diffusion coefficient, D_{Gr},

- (3) the fuel channel radius, r_{fc}.

These are all fed into block (10), which generates the *base graphite stringer matrix*. The base graphite stringer matrix is the first three matrices that are generated to solve radial coordinates, partial differential equation,

$$\frac{\partial C_{Xe}}{\partial t} = \frac{D_{Gr}}{\epsilon} \left(\frac{\partial^2 C_{Xe}}{\partial r^2} + \frac{1}{r} \frac{\partial C_{Xe}}{\partial r} \right) - (\phi \sigma_a^{Xe} + \lambda_{Xe}) C_{Xe}, \qquad (2.18)$$

where the shorthand $C_{Xe} = C_{Xe}^{Gr}(r, t)$ has been adopted. The left hand boundary condition is a zero flux condition,

$$\left(\frac{\partial C_{Xe}}{\partial r} \right)_{r=0} = 0, \qquad (2.19)$$

and the right hand boundary condition is a robin condition prescribing the mass transfer into the stringer,

$$\left(\frac{\partial C_{Xe}}{\partial r} \right)_{r=r_{fc}} = k_m \left(C_{FS} - \frac{HRT}{\epsilon} C_G \right). \qquad (2.20)$$

The solution uses a 20 node, right hand side ghost node, second order finite difference (FDM) decomposition with the method of lines to convert the partial differential equation into a series of 21 ordinary differential equations that can be solved by Simulink. The spatial decomposition of the graphite stringer is

radial with each node at a uniform distance of,

$$\Delta r = \frac{r_{fc}}{20}. \tag{2.21}$$

Furthermore, the node positions are indexed by,

$$r_i = i\Delta r, \tag{2.22}$$

such that $i \in [0, 21]$. The extra index (21) is to allow for the inclusion of the RHS ghost node. Denote N to be the index of the final node, 21.

In order to decouple the temperature dependent behavior of the right hand side boundary condition from the rest of the equation, it is partially implemented in a separate additive matrix H, represented by block (14) — described later. The reaction term, of Equation 2.18 is implemented through the B matrix (where B $= (\phi\sigma_a^{Xe} + \lambda_{Xe})$, in contrast to constant A on the base matrix), shown in block (18) – also described later. These three matrices, the base matrix (10), additive matrix H (14), and additive matrix B, are all added together through summation block (15) before fed to the rest of the system.

In regards to block (10), the base matrix, let us, for convince, define,

$$A \stackrel{def.}{=} \frac{D_{Gr}}{\epsilon}, \tag{2.23}$$

The first three entries of row 1 in the base matrix matrix are,

$$M_1 = \begin{bmatrix} -\frac{5A}{4\Delta r^2} \\ \frac{A}{\Delta r^2} \\ \frac{A}{4\Delta r^2} \end{bmatrix}^T \tag{2.24}$$

.

The first five entries of the second row of the base matrix are,

$$
M_2 = \begin{bmatrix}
\frac{A}{\Delta r^2} - \frac{A}{3\Delta r r_2} \\[2mm]
\frac{-2A}{\Delta r^2} - \frac{A}{2\Delta r r_2} \\[2mm]
\frac{-A}{\Delta r^2} + \frac{A}{2\Delta r r_2} \\[2mm]
\frac{-A}{\Delta r^2} + \frac{A}{2\Delta r r_2} \\[2mm]
\frac{A}{6\Delta r r_1}
\end{bmatrix}^T
\tag{2.25}
$$

Rows [3,18] are generated with,

$$
M_i = \begin{bmatrix}
\frac{-A}{12\Delta r^2} + \frac{A}{12\Delta r r_i} \\[2mm]
\frac{4A}{3\Delta r^2} - \frac{2A}{3\Delta r r_i} \\[2mm]
\frac{-5A}{2\Delta r^2} \\[2mm]
\frac{4A}{3\Delta r^2} + \frac{2A}{3\Delta r r_i} \\[2mm]
\frac{-A}{12\Delta r^2} - \frac{A}{12\Delta r r_i}
\end{bmatrix}^T ,
\tag{2.26}
$$

where i is the row number, and the insertion is performed beginning at column i.

The second last row, row 19 is generated with

$$
M_{N-1} = \begin{bmatrix}
\frac{-A}{12\Delta r^2} - \frac{A}{12\Delta r r_{N-1}} \\[2mm]
\frac{A}{3\Delta r^2} + \frac{A}{2\Delta r r_{N-1}} \\[2mm]
\frac{A}{2\Delta r^2} - \frac{3A}{2\Delta r r_{N-1}} \\[2mm]
\frac{-5A}{3\Delta r^2} + \frac{5A}{6\Delta r r_{N-1}} \\[2mm]
\frac{11A}{12\Delta r^2} + \frac{A}{4\Delta r r_{N-1}}
\end{bmatrix}^T ,
\tag{2.27}
$$

and is inserted starting at column 16 (N-5).

The final row is inserted starting at column 16 (N-5), and is,

$$
M_N \begin{bmatrix} \frac{-A}{12\Delta r^2} \\[6pt] \frac{A}{3\Delta r^2} \\[6pt] \frac{A}{2\Delta r^2} \\[6pt] \frac{-5A}{3\Delta r^2} \\[6pt] \frac{11A}{12\Delta r^2} \end{bmatrix}^T \quad . \tag{2.28}
$$

The final composition of these matrices is shown in Equation 2.6.

$$M = \begin{bmatrix}
M_{11} & M_{12} & M_{13} & M_{14} & M_{15} & 0 & \cdots & \vdots & 0 \\
0 & M_{21} & M_{22} & M_{23} & M_{24} & M_{25} & \cdots & \vdots & 0 \\
0 & \cdots & M_{i1} & M_{i2} & M_{i3} & M_{i4} & M_{i5} & \vdots & 0 \\
\vdots & \vdots & \vdots & \vdots & \cdots & \cdots & \cdots & \vdots & \cdots \\
0 & \cdots & \vdots & \vdots & 0 & M_{(N-1)1} & M_{(N-1)2} & M_{(N-1)3} & M_{(N-1)4} & M_{(N-1)5} \\
0 & \cdots & \vdots & \vdots & 0 & M_{N1} & M_{N2} & M_{N3} & M_{N4} & M_{N5}
\end{bmatrix}$$

(2.29)

Region	Flux ($\mathrm{m^{-2}\,s^{-1}}$)
1	7.49×10^{17}
2	6.35×10^{17}
3	2.03×10^{17}
4	1.30×10^{17}

Table 2.9: Graphite Region Neutron Fluxes

Block (14) generates additive matrix H which is a 21x21 zero matrix with element (N,N-1) set to 1. The H matrix is multiplied by (4), T, the graphite temperature, (5), Henry's constant, H_{Xe}, and (11), R, the ideal gas constant (HRT). The H matrix is also divided by (1), the graphite porosity, which is inverted through block (12).

The B matrix, supplied by block (18), is a 21x21 identity matrix with element (1,1) set to zero and element (N,N-1) set to 1. The B matrix (B for burnout) is multiplied by the reaction rate, which is the product, (18), of the neutron flux, ϕ, (7), and the neutron absorption cross section, σ_a^{Xe}, (8). The Xe-135 decay constant, λ_{Xe}, is added to the reaction rate, and this total is multiplied by the B-matrix before being added to the H matrix and the base matrix through block (15). Each graphite region has its own neutron flux which were set to values taken from ORNL-TM-0378 [24], page 23, and these values are shown in Table 2.9.

The output of the matrix summation, block (15) is fed into a matrix multiplication block, (22), which multiplies the resultant matrix of block (15) with a vector representing the concentration of xenon in each node of the FDM decomposition, (26).

In order to complete the solution to the FDM decomposition, the non-homogeneous term needs to be injected (added) to the result of the matrix multiplication, and this is done through summation block (26). Block (23)

compiles a vector,

$$
\begin{bmatrix}
0 \\
\vdots \\
\frac{r_{ghost}}{k_m}
\end{bmatrix},
\tag{2.30}
$$

to the solution, where k_m is the mass transfer coefficient supplied by block (6), which was supplied by block (4) in Figure 2.10. The other term, r_{ghost}, is the ghost node radius, which is placed Δr beyond the radius of the graphite stringer, $r_{ghost} = r_0 + \Delta r$.

Block (24) compiles the vector,

$$
\begin{bmatrix}
0 \\
\vdots \\
\frac{N_{Xe}^{FS}}{V_L^{FS}}
\end{bmatrix},
\tag{2.31}
$$

, where N_{Xe}^{FS} is the fuel salt xenon content, provided by block (20) through the fuel salt sub system described in Section 2.3, and V_L^{FS} is the fuel salt liquid content, provided through block (21) which is fed by the sum of all the liquid volumes generated in the thermophysical property subsystem, described in Section 2.4.

These terms are multiplied together by block (25.A) before being added to summation block (25).

Finally, the output for this subsystem are, (36), the graphite stringer mean Xe-135 concentration, C_{Gr}^{Xe}, and, (7), the graphite stringer Xe-135 mass flux out, J. The mean graphite stringer concentration is calculated through the a volume weighted average of the xenon concentration in each FDM node,

$$
\frac{\sum_i V_G^i C_{Xe}^i}{\sum_i V_G^i},
\tag{2.32}
$$

where $\vec{C}_{Xe} = [C^0_{Xe}...C^N_{Xe}]$ (these are graphite concentrations, the Gr super-script is dropped for convenience) is supplied through block (26) and $vecV_G = [V^0_G...V^N_G]$ are the volumes of each FDM node, generated through block (32). The mathematical operations for the averaging operation are provided through blocks (31), (32), (33), (34), and (35) respectively.

Mass transfer out of the graphite stringer, J, is handled through line (37). It is calculated through,

$$J = k_m \left(C^{Xe}_{FS} - \frac{HRT}{\epsilon} C^{Xe}_G \right). \tag{2.33}$$

The mass transfer coefficient, k_m, is supplied through block (6). The coefficient to the graphite xenon concentration stringer, $\frac{HRT}{\epsilon}$, is supplied by the output of block (13). The fuel salt xenon concentration is supplied by block (24) which calculates $C^{Xe}_{FS} = \frac{N^{FS}_{Xe}}{V^{FS}_L}$, where the fuel salt xenon content, N^{FS}_{Xe}, is supplied through block (26) and the fuel salt liquid volume, V^{FS}_L, is supplied through block (21). The graphite xenon concentration, C^{Xe}_G used in this mass transfer equation is taken to be the right most node xenon concentration, selected by block (27). Blocks (26), (29), and (30) supply the mathematical machinery to calculate the mass transfer flux, J.
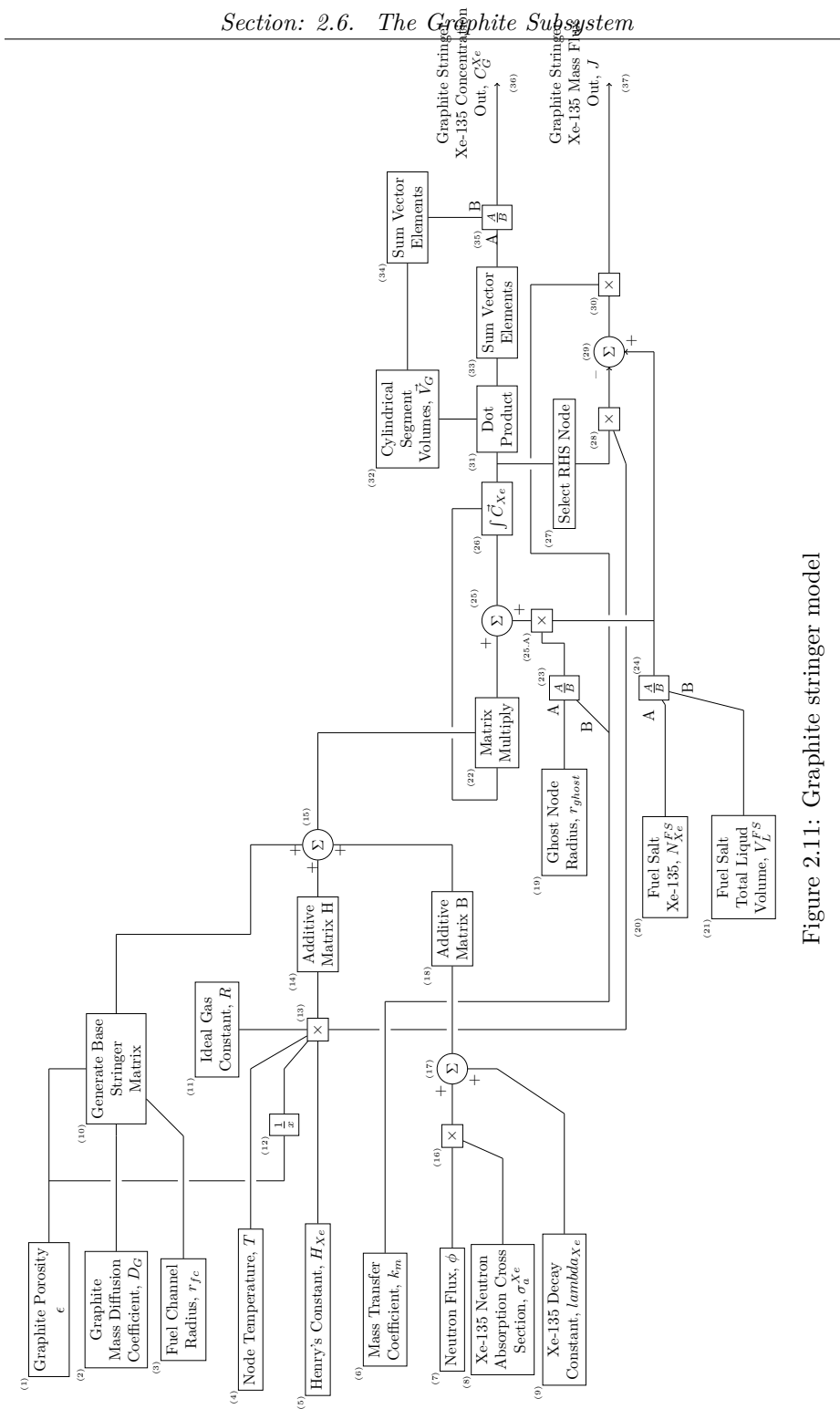
Figure 2.11: Graphite stringer model

2.7   The Bubble Subsystem

The top layer of the bubble model subsystem is illustrated in Figure 2.12. The four processes that affect the mass balance in the bubble subsystem are (1) mass transfer between the fuel salt and the bubbles, (2) burnout, (3) radioactive decay, and (6) removal of Xe-135 from the bubbles via the xenon stripper. These source/sink terms are summed through block (4), before being passed into scalar integrator (7). The coalescence and breakup rates are assumed sufficiently frequent to allow for the Xe-135 content in all bubbles to be represented by a single integrator.

The operation of the burnout block, (2), is similar to the operation of the burnout block in the fuel salt subsystem (Section 2.3), except the normalization volume in the total volume of circulating voids in the system, V_{CV}^{Tot}, which is found by summing the circulating void volumes in each lumped volume node, and the volume of reaction in the volume of circulating voids in the core, V_{CV}^{IC}, which is found by summing all of the circulating void volumes of the in core lumped volumes. The operation of the decay block, (3), is also identical to the operation of the decay block in the fuel salt subsystem (Section 2.3). The operation of the xenon stripper bubble removal block, (6), is provided by the xenon stripper subsystem and is described in detail in Section 2.8.

The operation of the mass transfer block, (1) in Figure 2.12, is shown in detail in Figure 2.13, which is now discussed. The purpose of the bubble mass transfer subsystem is to calculate the rate of change of Xe-135 content in the bubbles due to mass transfer processes, $\dot{N}_{Xe}^{B}$, and output this through line (14).

Essentially, the system solves an equation of the form,

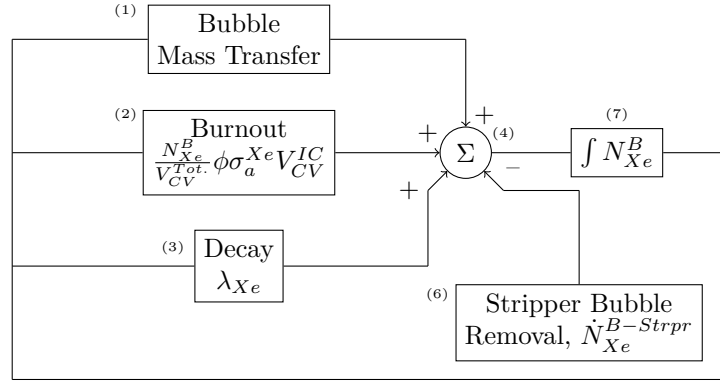$$\dot{N}_{Xe}^{B} = k_m A (C_{FS}^{Xe} - HRTC_B^{Xe}). \tag{2.34}$$

Figure 2.12: Bubble model subsystem

The $k_m A$ term is the total mass transfer coefficient and area and it is calculated for every node before being summed to get the total $k_m A$ term. This system is described in detail later.

Blocks (1), (2), and (8) calculate the C_{FS}^{Xe} term. Block (2) is the total liquid volume and is found by summing the liquids volumes of the individual nodes. Blocks (3), (4), and (9) calculate the C_B^{Xe} term. The fuel salt Xe-135 content, N_{Xe}^{FS}, block (1), is passed in from the fuel salt subsystem (see Section 2.3). The bubble Xe-135 content, N_{Xe}^B, block (3), is passed in from the bubble model subsystem (see Figure 2.12).

The coefficients to the C_B^{Xe} term, HRT, are taken from the thermophysical property subsystem (see Section 2.4). Henry's constant, H_{Xe}, is provided through block (7) which takes its temperature from the node temperature block, T, block (5). Finally, block (6), provides the ideal gas constant, R, and these constants are combined with the C_B^{Xe} term from block (9) through block (10).

Summation block (11) calculates the difference between the two previously described terms before being multiplied by the bubble mass transfer coefficient and area, $k_m A$, form block (13) through block (12), and the result is output through line (14).
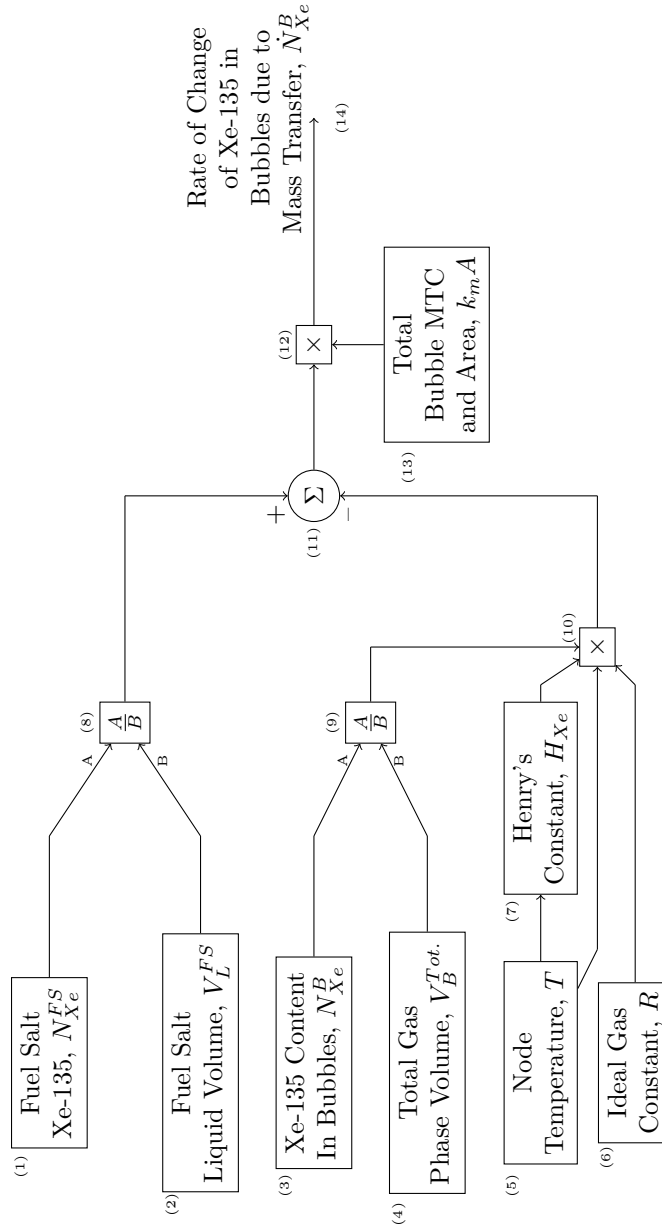
Figure 2.13: Bubble mass transfer subsystem

The subsystem that determines the bubble mass transfer coefficient and area, $k_m A$, is shown in Figure 2.14. For all of the proceeding calculations, bubbles are assumed sufficiently spherical to be represented by a spherical bubble model and this spherical bubble model is parameterized by a bubble radius, r_b, which is nominally set to $0.254\,\text{mm}$. The surface area of a single bubble, A_B^1, is calculated [add reference] through block and the single bubble volume, V_B^1, is calculated through node (3). Both of these calculations use the nominal bubble radius, r_b. Node (2) is the node gas volume, V_G, and this is divided by the single bubble volume, block (3) by block (5) to determine the number of bubbles in the node. The number of bubbles is then multiplied by the surface area of a single bubble, from block (1), the get the total bubble surface area in the node.

The method to calculate the mass transfer coefficient is dependent on the node in which the mass transfer coefficient is being calculated. The mass transfer correlations used to calculate the mass transfer coefficient are shown in Table 2.10. The mass transfer correlation is implemented in block (7) which derives its dimensionless numbers and thermophysical properties from the thermophysical property subsystem (Section 2.4).
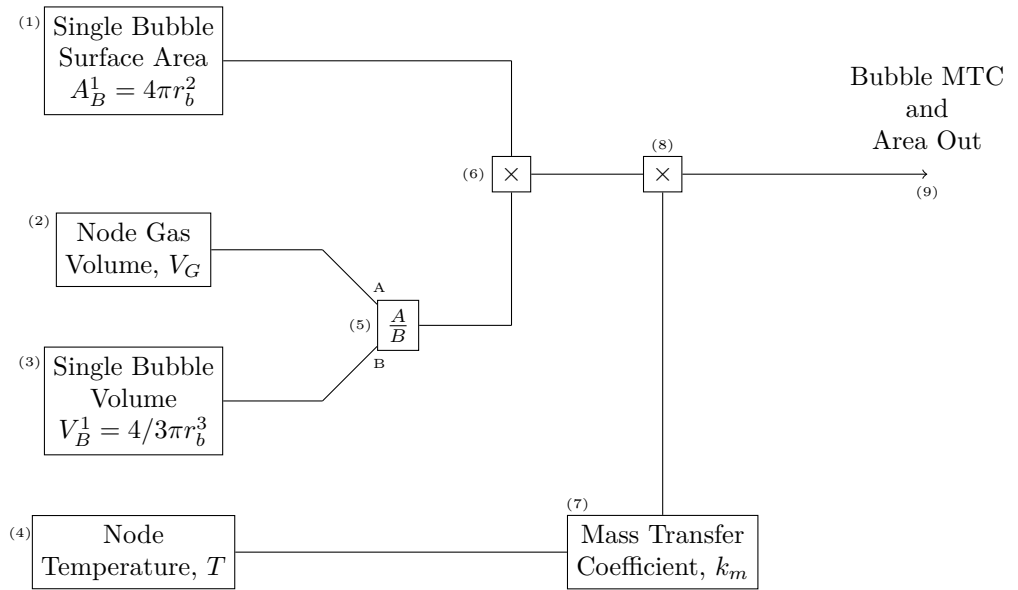
Figure 2.14: Subsystem to determine a node's bubble mass transfer area and mass transfer coefficient

Description	Correlation	Nodes Applied To	Notes	Source
Single bubbles of gas in liquid, continuous phase coefficient, very small bubbles	$\frac{k_m 2r_b}{D} = 1.0(ReSc)^{1/3}$	CA, UH, LH	r_B: bubble radius.	Perry's Handbook [26]page 5-69
Small rigid particles in turbulent pipeline flow	$\frac{k_m 2r_p}{D} = 0.0096Re^{0.931}Sc^{0.346}$	G_1–G_4, P_{100}–P_{102}, HX	r_p: pipe radius	ORNL-TM-2245page 23 [27]
Highly agitated systems; solid particles, drops, and bubbles; continuous phase coefficient	$k_m = \frac{0.13}{Sc^{2/3}}\left(\frac{(P/V)\mu g}{\rho}\right)^{1/4}$	FP	V: Tank volume, the volume of the pump bowel. P: Pump power	Perry's Handbook [26]page 5-70

Note: The pump power, P, is nominally 47.5 HP (35.4kW) and is taken from ORNL–TM–0728 [17]page 151. The tank volume, V, is the sum of the fuel pump gas and liquid volumes as well as the sum of the excess volumes from all other lumped volume nodes.

Table 2.10: Bubble mass transfer correlations used in dynamic model

2.8   The Xenon Stripper Subsystem

The operation of the xenon stripper is shown in Figure 2.15. The system has two outputs, the rate of removal of Xe-135 from the fuel salt, $\dot{N}_{Xe}^{FS\ Strpr.}$, provided through line (18), and the rate of removal of xenon from the bubbles, $\dot{N}_{X}e^{B\ Strpr.}$, line (16). Both of these mechanisms are dependent on *stripping efficiency*, η_B, and η_{FS} for the bubble and fuel salt stripping efficiency respectively and the effacing used in this model are derived from the data presented on page 50 of ORNL-4069 [20].

The rate of removal of xenon from the fuel salt is calculated through,

$$\dot{N}_{Xe}^{FS.\ Strpr.} = \eta_{FS} C_{Xe}^{FS} \dot{Q}^{Strpr.}, \tag{2.35}$$

where η_{FS} is the fuel salt stripping efficiency, provided by block (15), $\dot{Q}^{Strpr.}$ is the volumetric flow rate of fuel salt through the xenon stripper, provided by block (3), and C_{Xe}^{FS} is the fuel salt xenon concentration, which is provided by the computation of block (11). Block (5), the fuel salt Xe-135 content, N_{Xe}^{FS}, is provided by the fuel salt subsystem (Section 2.3). Block (6), the the total fuel salt liquid volume, is found by summing all the liquid volumes in all the nodes in the lumped volume sub system (Section 2.5). The fuel salt stripping efficiency, η_{FS}, is nominally set to 10%.

The bubble Xe-135 stripping action is output through line (17) and is calculated through,

$$\dot{N}_{Xe}^{B.Strpr.} = \eta_B C_B V_B^1 \dot{Q}^{Strpr.} C_{Xe}^B. \tag{2.36}$$

The bubble stripping efficiency, η_B, is provided by block (14), and is nominally set to 12%. The bubble concentration, C_B, is provided by the operation of by (9) and is the number of bubbles in the fuel salt per unit volume. Block (8)

provides the total number of bubbles in the fuel salt by dividing the total gas volume in the fuel salt, V_G^{FS}, provided by block (2), by the volume of a single bubble, V_B^1, provided by block (3). Summation block (10) provides the total fuel salt volume (both liquid and gas phases). Block (12) does the computation and line (16) provides the output.

The output of the bubble action, (16), is fed into the bubble subsystem whereas the output of the fuel salt action, (17), is fed into the fuel salt subsystem.
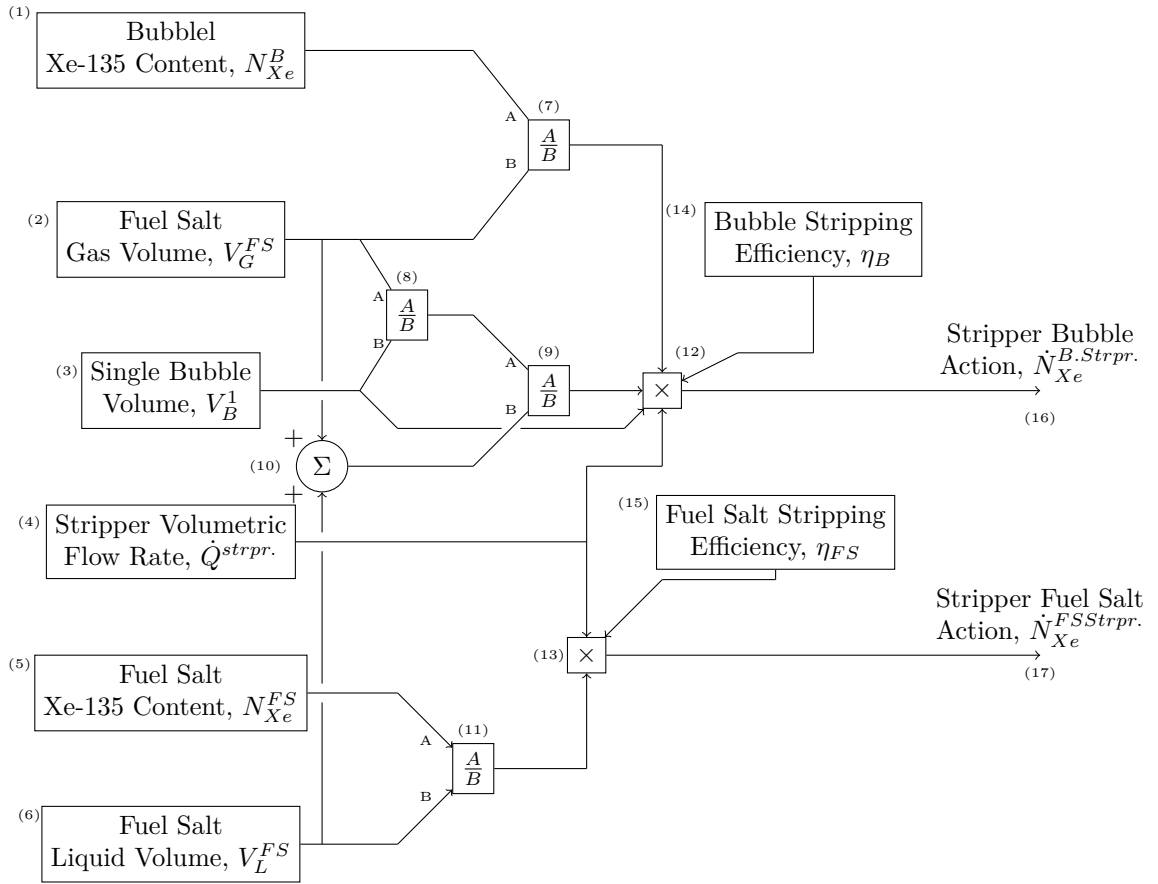

Figure 2.15: Xenon stripper system

2.9   Nuclear Properties and Reactivity Coefficients

Xenon concentration in both the fuel salt and graphite are converted to reactivity defects through reactivity coefficients. The reactivity coefficients, taken from page 54 of ORNL-TM-3464 [13], are shown in Table 2.11. The fuel salt reactivity coefficient was applied to both the fuel salt and bubble Xe-135 content. The combined fuel salt and bubble xenon concentration was calculated through,

$$\frac{N_{Xe}^{B} + N_{Xe}^{FS}}{V_{L}^{FS} + V_{G}^{FS}}. \tag{2.37}$$

Region	Reactivity Coefficient $(\frac{\delta k}{k} \frac{atoms}{cm^3})$
Combined Fuel Salt + Bubble	5.17×10^{-18}
Graphite Region 1	3.34×10^{-18}
Graphite Region 2	6.99×10^{-18}
Graphite Region 3	6.69×10^{-18}
Graphite Region 4	7.91×10^{-19}

Table 2.11: Dynamic model reactivity coefficients

2.10   Summary and Chapter Conclusion

This chapter has presented an overview of the inner workings of the dynamic model. The approach taken in this model is new in several aspects. Foremost, the model analyzes all thermophysical properties, lumped volumes, mass transfer constants as functions of temperature and this allows for dynamic analyses to be performed. Second, the bubble model of the MSRE is the most complete developed to date — the ORNL-TM-3464 [13] bubble model only included 5 regions whereas this model more than doubles that. Furthermore, this is the first time a graphite stringer has been modeled as a second order solution to a reaction diffusion equation and done so using multiple flow regions. Finally, the

nuclear data used includes the proper half life for Te-135, which was not done in prior MSRE xenon models, since the half life was not known at the time.

Nomenclature

Alphabetic and Greek Symbols	
$\dot{N}$	Rate of change of isotope i quantity
γ	Fission yield of isotope i
ϕ	Neutron flux
Σ	Macroscopic Neutron Absorption Cross Section
V	In core volume
λ	Decay Constant
t	Time
T	Temperature
Sc	Schmidt Number
k	Constant / Coefficient
r	Radius
f	Fraction
U	Velocity
Re	Reynolds Number
J	Mass Flux
ϵ	Porosity
A	Constant, $A = D_{Gr}/\epsilon$
M	Matrix
R	Ideal gas constant
η	Efficiency

Subscripts and Superscripts

i	Isotope or Node Index
f	Fission
Te	Te-135
Xe	Xe-135
IC	In Core
$1/2$	Half-Life
L	Liquid
G	Gas/
$[{}^\circ C]$	degrees Celsius
$[K]$	Kelvin
FS	Fuel Salt
μ	Viscosity
D	Mass diffusion coefficient
b	bubble
ρ	Mass Density
$MSRE$	Molten Salt Reactor Experiment Reference Value
A	Fitting Constant A
B	Bubble/ Fitting Constant B
C	Fitting Constant C
$Mes.$	Reference Measurement
CP	Concentration-Pressure Varient
CC	Concentration-Concentration Varient
0	Nominal Value
$Tot.$	Total
CV	Circulating Void
ref	Reference
1	State 1/ Single
2	State 2
m	Mass
fc	Fuel Channel
Gr	Graphite
a	Absorption
N	Ultimate index
$ghost$	Ghost node
$Strpr.$	Stripper

Bibliography

[1] M. Eades, E. Chaleff, P. Venneri, and T. Blue. The Influence of Xe-135m on Steady-State Xenon Worth in Thermal Molten Salt Reactors. *Progress in Nuclear Energy*, 93:397–405, 2016.

[2] A. Weinberg. *The First Nuclear Era: The Life and Times of a Technological Fixer*. American Institute of Physics, 1994. ISBN 9781563963582.

[3] B. Hoglund. MoltenSalt.org, 2012. URL `http://moltensalt.org/`. Last Accessed 9/5/2018.

[4] D. LeBlanc. Molten salt reactors: A new beginning for an old idea. *Nuclear Engineering and Design*, 240(6):1644–1656, 2010. ISSN 00295493. doi: 10.1016/j.nucengdes.2009.12.033.

[5] J. Serp, M. Allibert, O. Beneš, S. Delpech, O. Feynberg, V. Ghetta, D. Heuer, D. Holcomb, V. Ignatiev, J. Kloosterman, L. Luzzi, E. Merle-Lucotte, J. Uhlíř, R. Yoshioka, and D. Zhimin. The Molten Salt Reactor (MSR) in Generation IV: Overview and Perspectives. *Progress in Nuclear Energy*, 77:308–319, 2014.

[6] R. Rhodes. *The Making of the Atomic Bomb*. The Making of the Nuclear Age. Simon & Schuster, 1986.

[7] P. Pau, J. Berg, and W. McMillan. Application of stokes' law to ions in aqueous solution. *Journal of Physical Chemistry*, 94(6):2671–2679, 1990.

[8] M. Blander, W. Grimes, N. Smith, and G. Watson. Solubility of Noble Gases in Molten Fluorides. II. In the Lif-NaF-LF Eutectic Mixtures. *The Journal of Physical Chemistry*, 63(7):1164–1167, 1959.

[9] W. Haynes, editor. *CRC Handbook of Chemistry and Physics, 97th Edition*. CRC Press, 2016.

[10] R. Svehla. R-132: Estimated viscosities and thermal conductivities of gases at high temperatures. Technical report, NASA, 1962.

[11] M. Born. *Atomic Physics: 8th Edition*. Dover Publications, 2013.

[12] Terry Price, Ondrej Chvala, and Robert Z Taylor. Molten salt reactor xenon analysis: Review and decomposition. *Journal of Nuclear Engineering and Radiation Science*, 2019.

[13] J. Engel and R. Steffy. ORNL-TM-3464: Xenon Behavior in the Molten Salt Reactor Experiment. Technical report, Oak Ridge National Laboratory, Oak Ridge, TN, USA, 1971.

[14] A. Malinauskas, J. Rutherford, and R. Evans. ORNL-4148: Gas Transport in MSRE Moderator Graphite. Part 1: Review of Theory and Counter-diffusion Experiments. Technical report, Oak Ridge National Laboratory, 1967.

[15] R. Robertson. ORNL-TM-4541: Conceptual Design Study of a Single-Fluid Molten-Salt Breeder Reactor. Technical report, Oak Ridge National Laboratory, 1971.

[16] Jaakko Leppänen, Maria Pusa, Tuomas Viitanen, Ville Valtavirta, and Toni Kaltiaisenaho. The Serpent Monte Carlo code: Status, development and

applications in 2013. *Annals of Nuclear Energy*, 82:142–150, 2015. ISSN 18732100. doi: 10.1016/j.anucene.2014.08.024.

[17] R. Robertson. ORNL-TM-0728: MSRE Design and Operations Report. Technical report, Oak Ridge, TN, USA, 1965.

[18] Japan Atomic Energy Agency - Nuclear Data Center - Fission Product Yields, 2018. URL `https://wwwndc.jaea.go.jp/cgi-bin/FPYfig`. Last Visited 21/6/2019.

[19] E. Baum, H. Knox, and T. Miller. *Nuclides and Isotopes: Chart of the Nuclides*. Lockheed Martin, Bethesda, Maryland, United States, 16 edition, 2010.

[20] R. Kedl and A. Houtzeel. ORNL-4069: Development of a Model for Computing Xe-135 Migration in the MSRE. Technical report, Oak Ridge National Laboratory, Oak Ridge, TN, USA, 1967.

[21] S. Cantor, W. Cooke, S. Dworkin, D. Robbins, E. Thoma, and M. Watson. ORNL-TM-2316: Physical Properties of Molten-Salt Reactor Fuel, Coolant and Flush Salts. Technical report, Oak Ridge National Laboratory, Oak Ridge, TN, USA, 1968.

[22] G. Watson, R. Evans III, W. Grimes, and N. Smith. Solubility of Noble Gases in Molten Fluorides. In LiF-BeF2. *Journal of Chemical and Engineering Data*, 7(2):285–287, 1962.

[23] E B Nauman. *Chemical Reactor Design, Optimization, and Scaleup*. Wiley, Hoboken, NJ, USA, 2008. ISBN 9780470282069.

[24] P. Engel, J., Haubenreich. ORNL-TM-0378: Temperature in the MSRE Core During Steady-State Power Operation. Technical report, Oak Ridge National Laboratory, Oak Ridge, TN, USA, 1962.

[25] R. J. Kedl. ORNL-TM-3229: Fluid Dynamic Studies of the Molten-Salt Reactor Experiment (MSRE) Core. Technical report, Oak Ridge National Laboratory, Oak Ridge, TN, USA, 1970.

[26] R. Perry and D. Green. *Perry's Chemical Engineers' Handbook, Seventh Edition*. McGraw-Hill, New York, NY, USA, 7th edition, 2008.

[27] F. Peebles. ORNL-TM-2245: Removal of Xenon-135 from Circulating Fuel Salt of the MSBR by Mass Transfer to Helium Bubbles. Technical report, Oak Ridge National Laboratory, Oak Ridge, TN, USA, 1968.